

NNT : ***

n°LAL : ***

Thèse de doctorat

Search of the $0\nu\beta\beta$ decay with the SuperNEMO demonstrator

Thèse de doctorat de l'Université Paris-Saclay
préparée à l'Université Paris Saclay au sein du Laboratoire Irène-Joliot Curie
(anciennement Laboratoire de l'Accélérateur Linéaire)

École doctorale n°576 Particles, Hadrons, Energy, Nuclei, Instrumentation,
Imaging, Cosmos et Simulation (PHENIICS)
Spécialité de doctorat : Physique des particules

Thèse présentée et soutenue à Orsay, le ***, par

CLOÉ GIRARD-CARILLO

Composition du Jury :

Président

Rapporteur

Rapporteur

Christine Marquet
CENBG - Bordeaux-Gradignan

Examineur

Examineur

Examineur

Laurent Simard
LAL - Orsay

Directeur de thèse

Mathieu Bongrand
LAL - Orsay

Co-directeur de thèse

Contents

Contents	3
Introduction	7
1 Phenomenology of particle physics	9
1.1 The Standard Model of particle physics	9
1.1.1 Bosons	9
1.1.2 Fermions	9
1.1.3 $2\nu\beta\beta$ decay	9
1.1.4 Where the Standard Model ends	9
1.2 Going beyond the Standard Model with neutrinos	9
1.2.1 Neutrino flavors and oscillations	9
1.2.2 Neutrino masses and nature	9
1.2.3 Other searches beyond the Standard Model with neutrinos	9
1.3 $0\nu\beta\beta$ experiment status	9
1.3.1 Experimental design criteria	9
1.3.2 $0\nu\beta\beta$ direct search experiments	10
1.3.3 Bolometers	12
1.3.4 Time projection chambers	12
1.3.5 Scintillators	14
1.3.6 Tracking calorimeters	14
2 The SuperNEMO demonstrator	15
2.1 Demonstrator design	15
2.1.1 Comparison with NEMO3 experiment	15
2.1.2 Experimental design	15
2.1.3 Sources	15
2.1.4 Tracker	15
2.1.5 Calorimeter	15
2.1.6 Calibration systems	15
2.1.7 Control Monitoring system	15
2.1.8 Electronics	15

2.2	The background of SuperNEMO	15
2.2.1	Internal background	15
2.2.2	External background	17
2.2.3	Background specifications	18
2.2.4	Measured demonstrator background levels	18
2.3	Magnetic field	18
2.4	The SuperNEMO software	18
2.4.1	Simulation	18
2.4.2	Reconstruction	18
2.4.3	Modifications of simulation software	18
2.5	Analysis tools	18
2.5.1	Internal probability	18
2.5.2	External probability	20
3	Sensitivity of the SuperNEMO demonstrator to the $0\nu\beta\beta$	21
3.1	The $0\nu\beta\beta$ signal and background model	21
3.1.1	The $0\nu\beta\beta$ signal	22
3.1.2	Inside detector backgrounds	22
3.1.3	External backgrounds	23
3.1.4	Amount of simulation	23
3.2	Event selection	24
3.2.1	Electron definition	25
3.2.2	Total energy spectrum	25
3.3	Demonstrator sensitivity to the $0\nu\beta\beta$ decay of ^{82}Se	27
3.3.1	Sensitivity to the $0\nu\beta\beta$ half-life	27
3.3.2	Limit on the effective neutrino mass	29
3.4	Impact of sources contamination levels on the sensitivity	30
3.4.1	Contamination levels	31
3.4.2	Optimisation of event selection	33
3.5	Impact of the magnetic field on the sensitivity	38
3.5.1	Simulations of the magnetic field inside the demonstrator and reconstructed track fit	39
3.5.2	Impact of the magnetic field on signal and background selections	40
3.5.3	Influence of the magnetic field on optical modules and reconstruction efficiency	42
3.5.4	Simulations with a non-uniform magnetic field	43
3.6	Searching for the Neodymium-150 $0\nu\beta\beta$ decay	44
3.6.1	Searching for the $0\nu\beta\beta$ of other isotopes	45
3.6.2	Sensitivity to the $0\nu\beta\beta$ of ^{150}Nd	45
3.7	The final detector sensitivity	47
3.8	Conclusion	48
4	Improvement of the rejection of the internal Thallium-208 background	51
4.1	Motivations	51
4.2	The internal ^{208}Tl background	52

4.2.1	The internal conversion process	53
4.2.2	Selection of ^{208}Tl disintegrations in the 2e channel	54
4.3	Rejection of ^{208}Tl with a time-of-flight criterion	55
4.3.1	The internal probability	55
4.3.2	The exponential probability for ^{208}Tl events	57
4.4	Event selection	59
4.4.1	Selection on particle detection times	59
4.5	Impact of ^{208}Tl rejection on the experiment's sensitivity	60
4.5.1	Influence of the calorimeter time resolution	60
4.6	Conclusions	63
5	Characterisation of the calorimeter time resolution	65
5.1	Interaction of particles in the SuperNEMO scintillators	66
5.1.1	Interaction of electrons	66
5.1.2	Interaction of photons	66
5.2	Measurement of the time resolution with a ^{60}Co source	67
5.2.1	Description of Cobalt 60 nucleus	68
5.2.2	Time response of optical modules	68
5.2.3	Final experimental design	71
5.2.4	Signal events selection	73
5.2.5	Background estimation	75
5.2.6	Detector efficiency	79
5.2.7	Determination of the individual timing resolution of each optical module	79
5.2.8	Conclusion	84
5.3	The Light Injection System	84
5.3.1	Light injection system commissioning	85
5.3.2	Time resolution of optical modules	85
6	Detector commissioning	87
6.1	Reflectometry analysis	87
6.1.1	Goal of the reflectometry analysis	87
6.1.2	Pulse timing: controlling cable lengths	88
6.1.3	Signal attenuation	93
6.1.4	Pulse shape analysis	95
6.1.5	Comparison with ^{60}Co	95
6.1.6	Conclusion	95
6.2	Calibrating the electronic boards	95
6.2.1	Principle	95
6.2.2	Measuring the time offset of front end boards	95
6.2.3	Results	95
6.3	Energy calibration of optical modules	95
6.4	Baseline studies	95
6.5	Light Injection System	95
	Conclusion	97

Bibliography	99
---------------------	-----------

Sensitivity of the SuperNEMO demonstrator to the $0\nu\beta\beta$

We present a study aiming to evaluate the SuperNEMO sensitivity to the $0\nu\beta\beta$ decay, and the corresponding effective neutrino mass. Studies of this kind have already been conducted, and the final detector, based on the NEMO-3 technology, is expected to exclude half-lives up to 1.2×10^{26} y (90% CL), with an exposure of 500 kg.y with Selenium sources¹ [8]. The SuperNEMO demonstrator were designed in order to assess the technical feasibility of such a large-scale detector. Its installation started in early 2015, at the Laboratoire Souterrain de Modane. With a reduced exposure of 17.5 kg.y, this demonstrator is expected to reach a sensitivity on the $0\nu\beta\beta$ process of 5.3×10^{24} y (90% CL) [9].

As was the case with its predecessor, a copper coil was designed to deliver a magnetic field inside the wire chamber, to bend the charged particles trajectories, hence making it possible to discriminate between electrons and positrons. However, studies lead by the collaboration determined that this field could be impacted by the detector material (especially by the calorimeter magnetic shields), producing notable variations in intensity and a loss of energy resolution [9][10]. We aim to explore the impact, on both the demonstrator and final detector sensitivity, of the presence of this magnetic field. The findings of this study participate in better understanding the detector performances. In a context of investigating the demonstrator and final detector's capabilities, different internal source contamination levels are considered. The topology of interest is the two electrons topology, and we use the total energy sum to discriminate the signal from the background events. Thanks to SuperNEMO tracking capabilities, extra topological informations are exploited to improve the final sensitivity. To go further, we also explore the possibility of studying the $0\nu\beta\beta$ decay of other $\beta\beta$ isotopes.

3.1 The $0\nu\beta\beta$ signal and background model

A full simulation of the demonstrator was performed, to determine the upper limit on $0\nu\beta\beta$ half-life that can be probed with SuperNEMO. Due to this we would

¹Supposing the $0\nu\beta\beta$ decay of ^{82}Se occurs through the exchange of a light Majorana neutrino.

take to simulate every background contribution, we choose a simplified model. Indeed, in addition to signal simulations, only the most harmful backgrounds to the $0\nu\beta\beta$ decay search were simulated.

3.1.1 The $0\nu\beta\beta$ signal

The SuperNEMO detector was designed to search for the never-observed $0\nu\beta\beta$ decay. In the following, we assume the underlying mechanism for this decay is the exchange of a light Majorana neutrino, the so-called mass mechanism (MM), as it is the most widespread. The hypothetical $0\nu\beta\beta$ signal would be detected as an excess of events in the region of interest, with respect to the predicted background contamination levels. Some 10^7 $0\nu\beta\beta$ events were simulated inside the source foils, using the DECAY0 software [13].

3.1.2 Inside detector backgrounds

We simulated numerous types of backgrounds that could mimic and hinder the search of the $0\nu\beta\beta$ signal.

3.1.2.1 Internal backgrounds

The so-called *internal backgrounds* stand for decays occurring inside the source foils, presenting the same signature as the $0\nu\beta\beta$ signal. These backgrounds are mainly the $2\nu\beta\beta$ decay undergone by the source isotope, as well as disintegrations of ^{208}Tl and ^{214}Bi inside the source foils.


The $2\nu\beta\beta$ process

In the full energy range, the allowed $2\nu\beta\beta$ decay stands as the dominant internal background type. The corresponding two-electrons energy sum spectrum is a continuum, whose ending point should stand at $Q_{\beta\beta} = 2.99$ MeV, but is subtly shifted by the detector's energy resolution. We simulated 10^7 events of this decay inside the source foils, in the full energy window. However, above a certain energy value, the number of $2\nu\beta\beta$ events decreases, which can lead to a lack of statistics in a energy region favourable for the search of $0\nu\beta\beta$ signal. To offset this effect, we simulated additional 10^7 of this decay on a slightly reduced energy range, that is to say above 2 MeV. The second set of simulations is normalised with the first one. In this way, the lack of $2\nu\beta\beta$ simulated events in the high-energy tail is avoided, without requiring too high computational resources.

Source foils contamination by natural isotopes

As described in Sec. 2.2.1, after sources purification, remaining natural isotopes such as ^{208}Tl or ^{214}Bi can still be present inside the foils, constituting the principal internal source of background, with the $2\nu\beta\beta$ decay. We simulated 10^7 decays for each of the two isotopes, inside the source foils.

3.1.2.2 Tracker contamination by natural isotopes


The presence of gaseous ^{222}Rn inside the tracker, mainly deposited on the tracker wires, can produce events similar to internal ones. In fact,  of the progeny of ^{222}Rn , the ^{214}Bi , can decay on (or near) a foil, and appear with a two-electron topology, becoming hard to distinguish from a double beta decay candidate. As this isotope is distributed throughout the whole tracking detection volume, we simulated a large quantity of this decay, that is to say 10^8 decays on the tracker wires.

3.1.3 External backgrounds

This background category was described in detail in Sec. 2.2.2. As a reminder, it is populated by the external γ -ray flux produced by radioactive isotope decays (mostly ^{40}K , ^{214}Bi and ^{208}Tl) in detector components or surrounding laboratory rocks, as well as neutron interactions in the external iron shield. As simulating external backgrounds would be very consuming in terms of computing resources due to their very low probability to produce two electrons ($2e$) topologies, let us check that these simulations are indispensable. The NEMO-3 experiment set a limit on the external background number of counts, of < 0.2 events in the $2e$ topology, for the energy range $[2.8; 3.2]$ MeV (two electrons energy sum), for an exposure of $34.3 \text{ kg}\cdot\text{y}$, with ^{100}Mo sources [14]. Recent radiopurity measurements of the SuperNEMO PMTs allow to conclude that the PMT ^{214}Bi activity is 35% lower than for those of NEMO-3 [15], which is encouraging. Unfortunately, these measurements also revealed that the PMT budget in ^{208}Tl isotope is 150% higher than NEMO-3. This could lead us to think that the external background contribution for SuperNEMO could be higher than that of NEMO-3. However, on that level, the most notorious difference between the two detectors is the fact that the SuperNEMO scintillator blocks are thicker than those of NEMO-3. Therefore, a gamma emitted from a PMT glass is more likely to be detected before crossing the source foils, such that it would be rejected and would not contribute to the background in the $2e$ channel. Even if the regions of interest are slightly different between these two experiments, it produces a negligible increase on the external background contribution². After all, given the fact that SuperNEMO is expected to be better than NEMO-3 at rejecting external background events, we consider that all external backgrounds from outside the foil, apart from ^{222}Rn in the tracking volume, are expected to be negligible, and were not simulated.

3.1.4 Amount of simulation

The number of natural isotope decay events expected in the $2e$ topology depends on their activities inside the source foils (for ^{208}Tl and ^{214}Bi), or on the tracker's wires (for ^{222}Rn decaying in ^{214}Bi). Therefore, it is mandatory to constrain

²A study conducted by the SuperNEMO collaboration shown that at most 0.73 additional external background events would have been expected for the NEMO-3 detector, if instead of taking the $[2.8; 3.2]$ MeV energy range, we would have considered the $[2.7; 3.15]$ MeV region of interest. 

the maximal tolerable activities for the detector [11]. The collaboration then established recommendations for maximum levels of the internal backgrounds, expressed in number of disintegrations per second, for a unit mass of $\beta\beta$ isotope, or for a unit volume of gas. These *specified activities* have been calculated in order to achieve the expected sensitivity of the final detector.

The amount of expected double β decays is driven by its half-life value: the higher the half-life, the lower its contribution in the total number of expected background. For this analysis, we consider the $2\nu\beta\beta$ half-life of ^{82}Se measured by NEMO-3, $T_{1/2}^{2\nu} = 9.39 \pm 0.17 \text{ (stat)} \pm 0.58 \text{ (syst)} \times 10^{19} \text{ years}$ [12]. For the $0\nu\beta\beta$ process, we also take the best limit set by the NEMO-3 detector, $T_{1/2}^{0\nu} > 2.5 \times 10^{23} \text{ y}$ [12]. This value is given for illustration purposes only, as it is not used to estimate the sensitivity of the detector.

Tab. 3.1 gives the expected number of signal and background events, for the demonstrator and final detector exposures. We also summarise the amount of

Process	Expected decays		Simulated decays
	Demonstrator	Final detector	
$0\nu\beta\beta$ ($T_{1/2}^{0\nu} = 2.5 \times 10^{23} \text{ y}$)	3.6×10^2	1.0×10^4	1.0×10^7
$2\nu\beta\beta$ ($T_{1/2}^{2\nu} = 9.39 \times 10^{19} \text{ y}$)	9.5×10^5	2.7×10^7	1.0×10^7
^{208}Tl ($\mathcal{A}^{\text{Tl}} = 2 \mu\text{Bq/kg}$)	1.1×10^3	3.1×10^4	1.0×10^7
^{214}Bi ($\mathcal{A}^{\text{Bi}} = 10 \mu\text{Bq/kg}$)	5.5×10^3	1.6×10^5	1.0×10^7
^{222}Rn ($\mathcal{A}^{\text{Rn}} = 0.15 \text{ mBq/m}^3$)	1.8×10^5	7.2×10^6	1.0×10^8

Table 3.1: Expected number of events for signal and background, for the demonstrator (17.5 kg.y) and for the final detector (500 kg.y). We assume target background activities are reached: $\mathcal{A}^{\text{Tl}} = 10 \mu\text{Bq/kg}$, $\mathcal{A}^{\text{Bi}} = 2 \mu\text{Bq/kg}$, $\mathcal{A}^{\text{Rn}} = 0.15 \text{ mBq/m}^3$. The measured half-life $T_{1/2}^{2\nu} = 9.39 \times 10^{19} \text{ y}$ for ^{82}Se is considered, and we assume $T_{1/2}^{0\nu} = 2.5 \times 10^{23} \text{ y}$ [12]. The total amount of simulation is also given.

simulated decays for this analysis. The expected number of disintegrations do not take into account any technique to reject background, and are given for the full energy range. Indeed, they are expected to be extremely reduced, notably by the application of event selections aimed at maximising the sensitivity to the $0\nu\beta\beta$ half-life. Moreover, for the current sensitivity analysis, we focus on a narrow energy window, called *region of interest*, whose usefulness is described in detail in Sec. 3.2. This is also one of the reasons why we have chosen to simulate a large number of events, so that the signal and backgrounds are correctly represented in the region of interest.

3.2 Event selection

For SuperNEMO, the $0\nu\beta\beta$ signature is two-electrons events, emitted simultaneously from the same vertex on the source foils, with an energy sum compatible with $Q_{\beta\beta} = 2.99 \text{ MeV}$ for ^{82}Se sources. Therefore, we conducted this analysis selecting only events matching the $2e$ topology.

3.2.1 Electron definition

To define what a two-electrons topology is, we should first define how an electron is defined. A reconstructed particle is tagged as an electron if it has

- a vertex on the source foil,
- a reconstructed track inside the wire chamber,
- an associated calorimeter hit,
- and a final criterion depending on the charged particle curvature. In fact, as announced, we aim at studying the influence of the magnetic field on the final sensitivity results. To this end, we are led to consider two separate cases, one where the magnetic field is switched on, aligned with the Z (vertical) axis of the detector, with a uniform value of 25 Gauss, and one where it is switched off (see details in Sec. 3.5). In the first case, particles such as electrons and positrons of a few MeV have a curved trajectory in the tracker. In the second case, the tracks of the particles may be similar to straight lines (not to mention the possible multiple scattering on the wires of the tracker). It is then necessary to adapt the selection of events to each case. When the magnetic field is on, we consider a fourth criterion: a particle is identified as an electron if its track has a negative curvature³. In the following, we present results where the magnetic field is turned on. The off-field study is addressed in Sec. 3.5.

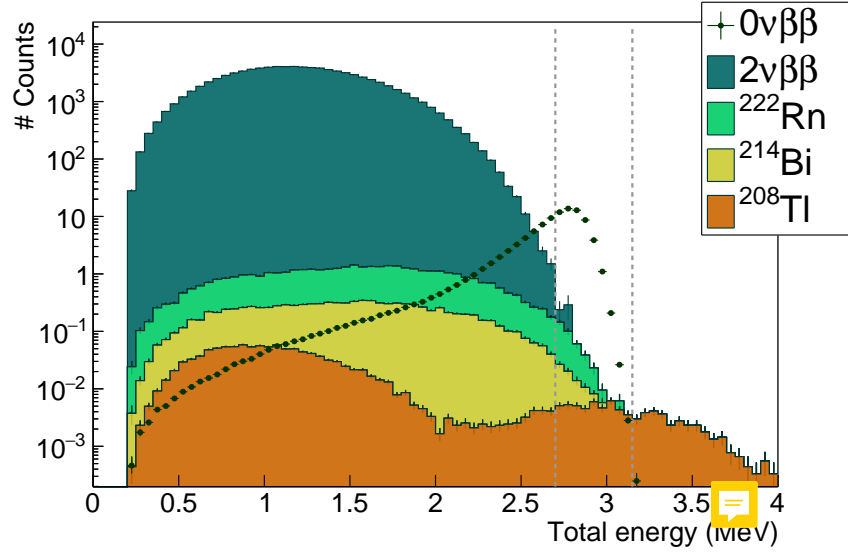
All these selections represent the so-called *first-order* cut-offs.

3.2.2 Total energy spectrum

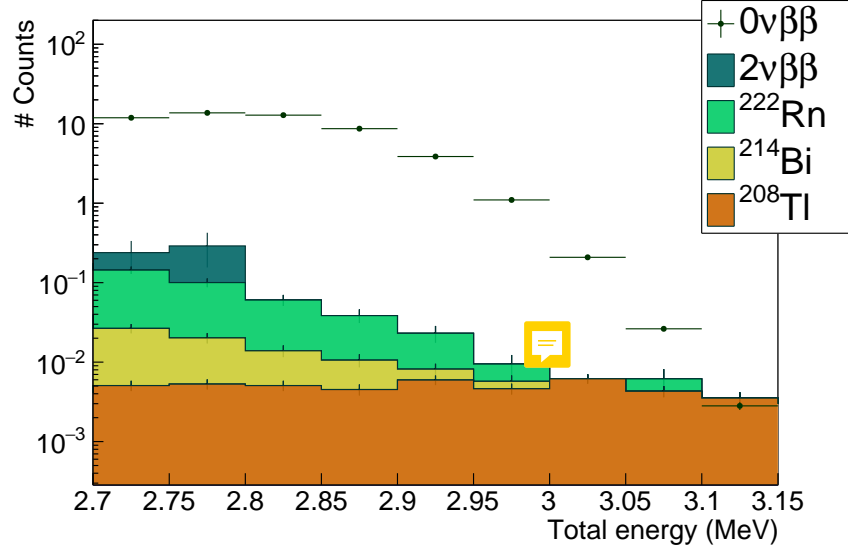
In Fig. 3.1, we present the total energy spectra for each simulated process in the $2e$ topology, after application of the first-order cut-offs. The distributions are given for the demonstrator (^{82}Se sources, 17.5 kg.y exposure), considering the specified activities are reached.

- If the $0\nu\beta\beta$ decay is detected, the two-electrons energy sum distribution would be a peak, located at the end-point of the $2\nu\beta\beta$ energy distribution, that is to say at the total available energy, $Q_{\beta\beta} = 2.99$ MeV. As the two electrons of this decay would share the total available energy, this peak should be infinitely thin. However, a widening of this distribution is expected, due to energy losses inside the dense source material. Indeed, the path of an electron in the source is more or less long, depending on the disintegration location, and the emission angle, leading to a degradation of the measured energy. This peak is also expected to be shifted towards small energies, by the calorimeter energy resolution and the straggling of energy losses inside the wire chamber. Consequently, the $0\nu\beta\beta$ energy distribution is expected to be asymmetrical, as displayed in the figure.

³A trajectory is said to be negative if it has the same curvature as that of an electron moving from the source to the calorimeter, in a magnetic field oriented according to $+Z$.



(a) Full energy range.



(b) Zoom on ROI.

Figure 3.1: Total energy spectra for the $0\nu\beta\beta$ signal and main backgrounds, for (a) the full energy range, and (b) for the $[2.7;3.15]$ MeV energy range, whose optimisation is discussed in Sec. 3.3. The $2\nu\beta\beta$ spectrum is normalised to $T_{1/2}^{2\nu} = 9.39 \times 10^{19}$ y, and the specified activities are considered for ^{208}Tl , ^{214}Bi and ^{222}Rn . The amplitude of the $0\nu\beta\beta$ is arbitrarily set at the limit obtained with NEMO-3.

- As explained in Sec. 3.1, we simulated two sets of $2\nu\beta\beta$ events: one on the full energy range, and one for which the two-electrons energy sum is greater than 2 MeV. After the normalisation of these two sets, we get the complete $2\nu\beta\beta$ energy spectrum displayed in the figure.
- The ^{208}Tl total energy spectrum extends up to high energies. It reveals two

distinct peaks, one corresponding to a low-energy β particle, the other to the internal conversion of the 2.614 MeV gamma ray, emitted after ^{208}Tl β^- disintegrations (Sec. 2.2.1).

- Whatever their origin, either ^{222}Rn contaminations inside the tracker gas, or internal contaminations of the source foils, the two ^{214}Bi energy distributions have nearly the same shapes.

These energy spectra confirm the $2\nu\beta\beta$ background is dominant in the total energy range. Therefore, a widespread technique consists in constraining the $0\nu\beta\beta$ decay searches to a narrow energy range, the so-called *region of interest* (ROI). It allows to reduce the total number background decays, while maximising the chances of observing the signal decay. A typical ROI is materialised in the figure by two vertical dashed lines, revealing ^{208}Tl , ^{214}Bi and ^{222}Rn could be harmful for the search of the $0\nu\beta\beta$ decay. The influence of the sources contamination by these natural isotopes, as well as optimised background rejection techniques are presented in Sec. 3.4.

In the following, we expose general principles leading to the determination of the best limit on $T_{1/2}^{0\nu}$, in the appropriate region of interest. We illustrate the reasoning by applying it on the demonstrator case, with specified activities, and on-magnetic field condition. However, the technique presented remain valid for all exposures, internal contamination levels and field conditions.

3.3 Demonstrator sensitivity to the $0\nu\beta\beta$ decay of ^{82}Se

The SuperNEMO demonstrator is designed to measure $\beta\beta$ decays of radioactive emitters. In case a the non-observation of the $0\nu\beta\beta$ process, the collaboration would set an upper-limit on the half-life $T_{1/2}^{0\nu}$, and on the effective neutrino mass $m_{\beta\beta}$.

3.3.1 Sensitivity to the $0\nu\beta\beta$ half-life

In case of the non-observation of a $0\nu\beta\beta$ signal, the expected upper limit on the half-life is provided for a given energy range $[E_{\min}; E_{\max}]$ on the two electrons energy sum, and depends on the characteristics of the detector. Firstly, it depends on the signal detection efficiency, $\epsilon_{0\nu}$, in this energy window. It also depends on the source isotope nature, as well as on the detector exposure $m \times t$, with m the mass of source material in the foils and t the data acquisition time period. It follows

$$T_{1/2}^{0\nu} > \frac{\mathcal{N}_A \ln 2}{M} \times \frac{\epsilon_{0\nu} \times m \times t}{N_{0\nu}^{\text{excl.}}}, \quad (3.1)$$

with \mathcal{N}_A the Avogadro number and M the $\beta\beta$ emitter molar mass. $N_{0\nu}^{\text{excl.}}$ is the number of signal events excluded, calculated with the Feldman-Cousins statistics from the total expected number of background events. The Feldman-Cousins statistics [16] is a wide-used method in rare events search experiments, providing

confidence intervals for upper limits in the case of background events following a Poissonian probability law. We use this method in the framework of this analysis to provide a limit, at 90% CL, on the number of excluded signal events $N_{0\nu}^{\text{excl.}}$, on the basis of the expected number of background events, given below.

- The $2\nu\beta\beta$ background

Eq. (3.1) defines the upper limit on $T_{1/2}^{0\nu}$ from the number of excluded signal events, and the signal selection efficiency $\epsilon_{0\nu}$. In a similar manner, we can define the number of expected $2\nu\beta\beta$ events, $N_{2\nu}$, from the half-life $T_{1/2}^{2\nu}$ and the $2\nu\beta\beta$ selection efficiency, $\epsilon_{2\nu}$, as

$$N_{2\nu} = \frac{N_A \ln 2}{M} \times \frac{\epsilon_{2\nu} \times m \times t}{T_{1/2}^{2\nu}}. \quad (3.2)$$

- Natural radioactive backgrounds

We consider the background massic activities $A_{\text{rad.}}$, and $\epsilon_{\text{rad.}}$ their selection efficiencies in a given energy window. The number of background events is therefore given, for the ^{208}Tl and ^{214}Bi internal contaminations, as

$$N_{\text{rad.}}^m = A_{\text{rad.}}^m \epsilon_{\text{rad.}}^m \times m \times t, \quad (3.3)$$

where $A_{\text{rad.}}$ is given in Bq/kg. Similarly, for the ^{222}Rn background,

$$N_{\text{rad.}}^V = A_{\text{rad.}}^V \epsilon_{\text{rad.}}^V \times V \times t, \quad (3.4)$$

with $V = 15.3 \text{ m}^3$ the total tracker volume, and $A_{\text{rad.}}$ represents here a volumic activity, given in Bq/ m^3 .

As we said, all equations from Eq. (3.1) to (3.4), are valid for a given energy range $[E_{\text{min}}; E_{\text{max}}]$. To find the optimal energy interval for the search of the $0\nu\beta\beta$ decay, that is to say the one maximising the limit on $T_{1/2}^{0\nu}$, we must study the influence of the variations of E_{min} and E_{max} bounds on the final sensitivity. On Fig. 3.1, we observe that beyond the energy sum of 3 MeV, the total number of background events is highly reduced, and the ^{208}Tl background dominates, with 0.03 count expected for $E > 3.2 \text{ MeV}$. This is why the upper limit E_{max} of the energy interval has only a limited impact on the search for the best ROI. It is then natural to study mainly the influence of the upper limit E_{min} . In that purpose, the selection efficiencies, entering in the calculation of the $T_{1/2}^{0\nu}$ upper limit, are presented in Fig. 3.2, as a function of the lower bound E_{min} . We remind the selection efficiency ϵ is the ratio of the number of selected events, to the number of simulated ones. As a matter of fact, the ROI would correspond to an energy range where $\epsilon_{0\nu}$ is high, and where selection efficiencies for the background are low, in order to maximise the $T_{1/2}^{0\nu}$. The variations of the limit set on $T_{1/2}^{0\nu}$ (at 90 % CL) as a function of E_{min} and E_{max} are presented in Fig. 3.3. We found that, for the demonstrator exposure, with ^{82}Se sources, with a 25 Gauss magnetic field, and for the specified background activities, the best ROI is $[2.7; 3.15] \text{ MeV}$. As expected, the upper bound does not impact the results for $E_{\text{max}} > 3.15 \text{ MeV}$, so this value is kept, in order to enter into a future more general study, taking

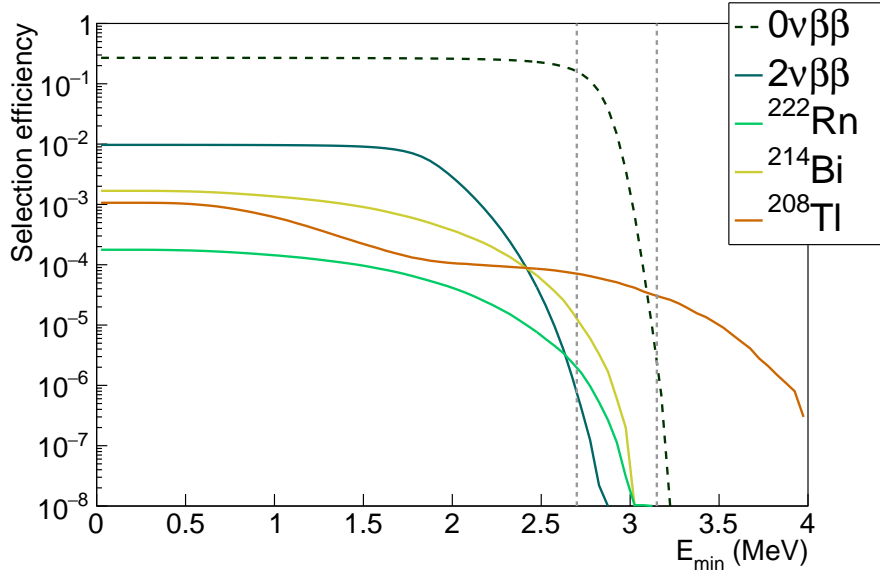


Figure 3.2: Efficiency spectra as a function of $E > E_{\min}$, for the $0\nu\beta\beta$ signal (dashed black line) and for the main backgrounds (plain lines). The two vertical grey lines depict the final ROI optimised for the case of the demonstrator, taken the specified isotope activities.

into account the external background of the experiment, which extend at high energies. In the optimised [2.7;3.15] MeV energy range, the sensitivity expected for the SuperNEMO demonstrator stands at

$$T_{1/2}^{0\nu} > 5.7 \times 10^{24} \text{ y} \quad (90\% \text{CL}). \quad (3.5)$$

This result is compatible with previous SuperNEMO analysis [9].

3.3.2 Limit on the effective neutrino mass

The decay rate for the light Majorana exchange mechanism is given by:

$$(T_{1/2}^{0\nu})^{-1} = g_A^4 G^{0\nu} |M^{0\nu}|^2 \left| \frac{m_{\beta\beta}}{m_e} \right|^2. \quad (3.6)$$

where $G^{0\nu}$ is the two particles phase space factor, depending on $Q_{\beta\beta}$ and Z the number of protons, $M^{0\nu}$ is the nuclear matrix elements for the $0\nu\beta\beta$ process, and $m_{\beta\beta}$ is the effective Majorana neutrino mass, defined as

$$\langle m_{\beta\beta} \rangle = \left| \sum_i m_i U_{ei}^2 \right|, \quad (3.7)$$

where m_i are the neutrino masses, and U_{ei}^2 is the mixing matrix. Therefore, the effective mass takes into account the neutrino mixing. Consequently, observing the $0\nu\beta\beta$ decay would not only prove the Majorana nature of neutrinos but, assuming the mass mechanism, could also help constraining the absolute neutrino masses. Given g_A , $G^{0\nu}$ and $M^{0\nu}$ [17][18][19][20][21][22][23][24][25][26], we find the SuperNEMO demonstrator could reach a limit on the effective neutrino mass of

$$\langle m_{\beta\beta} \rangle = [0.24 - 0.47] \text{ eV}. \quad (3.8)$$

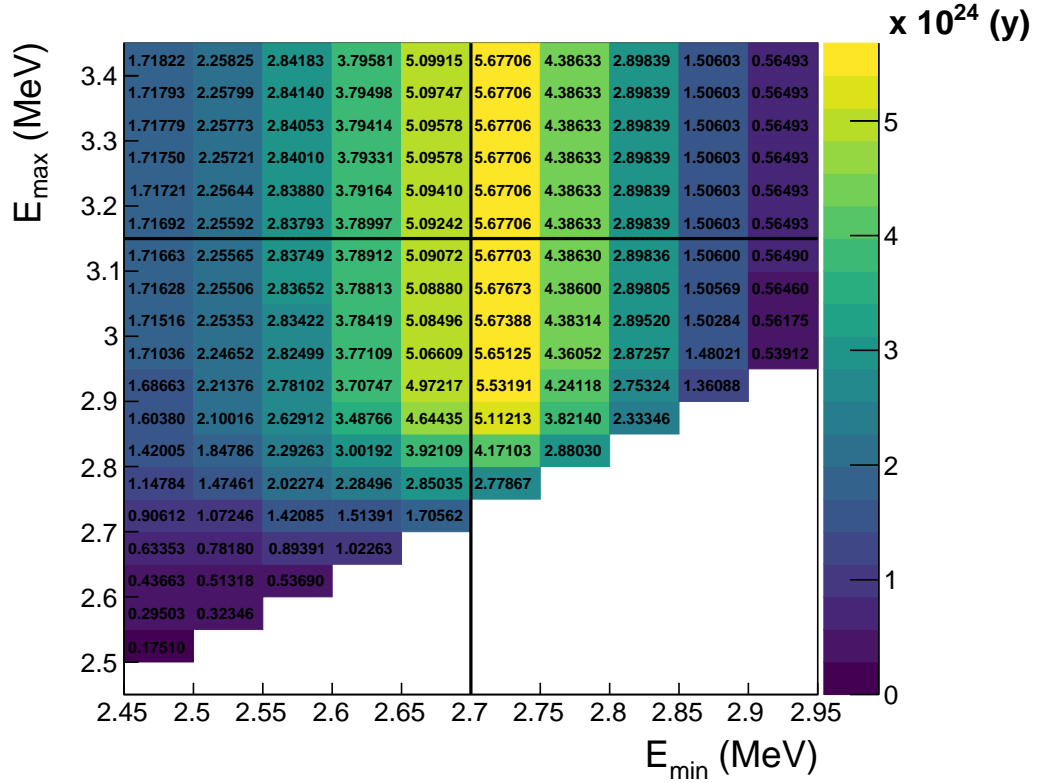


Figure 3.3: Two-dimensional histogram showing the evolution of the $T_{1/2}^{0\nu}$ value as a function of the lower and upper energy bounds. The maximum upper limit of $T_{1/2}^{0\nu} > 5.7 \times 10^{24}$ y (90% CL) is retained, in the $[2.7; 3.15]$ MeV region of interest.

Although this limit is not competitive with other current $0\nu\beta\beta$ experiments, it proves that SuperNEMO's technology would benefit from being adapted to larger scales.

In this section, we presented the general procedure leading to an optimised result on the $T_{1/2}^{0\nu}$ limit, and gave a result for the SuperNEMO demonstrator compatible with the previous studies led by the collaboration. Thereafter, we discuss the results obtained for different detector exposures (demonstrator and final detector), and different internal background activities. Also, and this is the main purpose of this study, we discuss the influence of the presence of the magnetic field on the final detector's sensitivity.

3.4 Impact of sources contamination levels on the sensitivity

We study the impact of the isotope contamination levels (inside the source foils, as well as on the tracker's wires) on the $0\nu\beta\beta$ sensitivity. We also optimise additional event selections aimed at improving it.

3.4.1 Contamination levels

From BiPo and SuperNEMO collaboration measurements (Sec. 2.2.1), we know that the targeted ^{208}Tl level is not reached, being almost 27 times higher than expected, with $\mathcal{A}^{\text{Tl}} = 54 \mu\text{Bq/kg}$ [26 - 102]. We also know that the ^{214}Bi contamination is not greater than $290 \mu\text{Bq/kg}$. If, unfortunately, this upper limit was reached, we would expect 1.6×10^5 internal bismuth events in the total energy range. Fortunately, the Radon contamination inside the wire chamber does not exceed the specifications. In Sec. 3.3, we developed the general procedure allowing to set a 90% confidence interval limit on $T_{1/2}^{0\nu}$. For the demonstrator, supposing the specified activities are reached, the demonstrator would achieve a sensitivity of 5.7×10^{24} years on the searched decay, in 2.5 years of data acquisition, with 7 kg of ^{82}Se . This sensitivity could be affected by the higher-than-specified levels of internal contaminations measured by BiPo.

In this sub-section, four distinct levels of internal contaminations are considered:

- the *zero activities* case, a hypothetical case where the source foils and the tracker are non contaminated at all by natural isotopes,
- the *specified activities* case, where the targeted level of contaminations would have been reached,
- and two *measured* cases, that takes into account the measured levels and limits on the contaminations at 90% CL. Indeed, as the ^{214}Bi activity is provided by BiPo measurements as an upper limit, it is possible for this level to be lower than $290 \mu\text{Bq/kg}$. We therefore choose to present the results either for sources that would not be contaminated by this isotope (the *without ^{214}Bi* case), or considering that the activity reached is $290 \mu\text{Bq/kg}$ (*with ^{214}Bi*).

The fact that we are showing results for a hypothetical zero isotope contamination is to illustrate an important phenomenon about the Feldman-Cousins statistics employed to determine the number of excluded signal events, $N_{0\nu}^{\text{excl.}}$, given the number of observed background events (defined from Eq. (3.2) to Eq. (3.4)).

Clarifications on Feldman-Cousins statistics When the expected number of background events is negligible (which is the case for the zero and specified levels), the probability p to observe n_s signal events, expecting s events, is given by the Poisson distribution

$$p = \frac{e^{-s} s^{n_s}}{n_s!} . \quad (3.9)$$

Let's now put ourselves in the situation where no signal event is observed - that is what we assume to put an upper limit on the $0\nu\beta\beta$ half-life. Then $n_s \rightarrow 0$, and $p \rightarrow e^{-s}$. If zero signal event is *observed*, it is incorrect to assume that zero signal events were *produced* during the experiment. We only can say that no signal event has been observed *a priori*. To account for this particular case, the quantity s should no longer be viewed as the number of expected signal events, but as the

3. SENSITIVITY OF THE SUPERNEMO DEMONSTRATOR TO THE $0\nu\beta\beta$

number of excluded signal events, $N_{0\nu}^{\text{excl.}}$. In the end, for a negligible expected number of background events, and no signal event observed, we can set an upper limit on the number of excluded signal events, excluding values for which $p < \alpha$. Taking a 90% confidence interval, that is to say $\alpha = 10\%$, we obtain $s \leq 2.303$.

We show in Fig. 3.4 the 90 % CL $T_{1/2}^{0\nu}$ limit for the four contamination levels considered, as well as the corresponding regions of interest, optimised following the technique explained in Sec. 3.3.. As expected from the previous conclusions

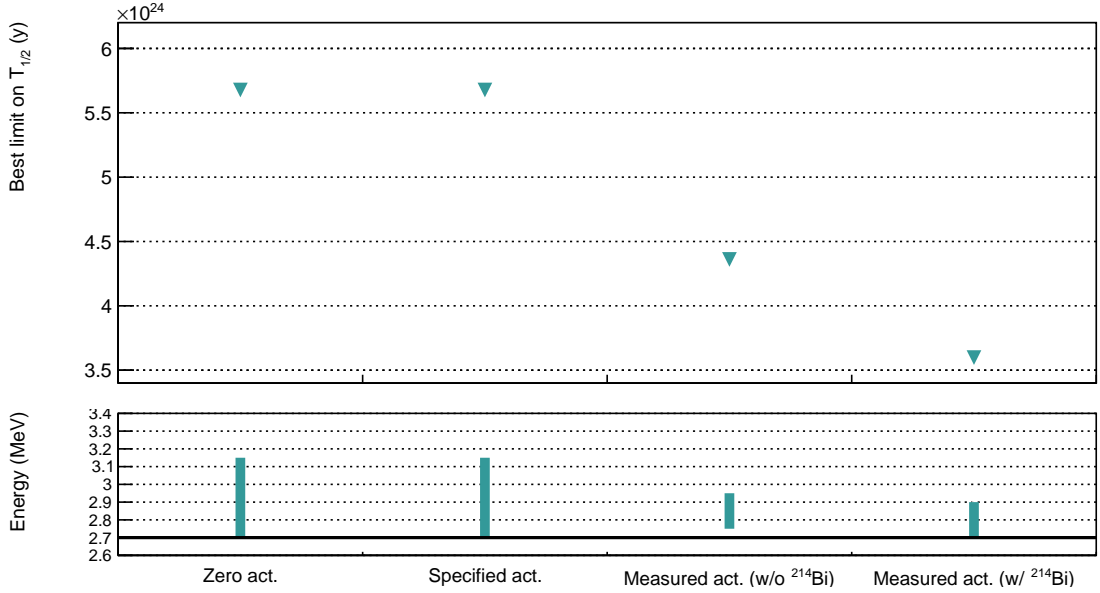


Figure 3.4: The 90% CL limit on the $0\nu\beta\beta$ half-life (top pad), and the corresponding ROI (bottom pad), as a function of the contamination level considered. For the *zero activities* case, we consider hypothetical contamination levels where $\mathcal{A}^{\text{Bi}} = \mathcal{A}^{\text{Tl}} = 0$ Bq/kg. The *specified activities* are presented in Tab. 2.1. The *measured activities*, provided by the BiPo detector [27], are presented in the same table. We consider successively a null ^{214}Bi contamination (*measured act. w/o ^{214}Bi*), or equals to the 290μ Bq/kg upper limit (*measured act. w/ ^{214}Bi*).

given on the Feldman-Cousins statistics, no difference is observed in terms of half-life limits, or ROI, between the zero and specified activity cases. Now considering the two measured activity cases, the sensitivity is decreased compared with the specified case. Indeed, the number of background events in the ROI is no more negligible, and influence significantly the value of $T_{1/2}^{0\nu}$, decreasing the experiment's sensitivity by 23% (without ^{214}Bi) and 37% (with ^{214}Bi).

Tab. 3.2 summarises the expected number of background events for each non-zero contamination case presented in Fig. 3.4. Regions of interest, optimised for each activity, are reminded. The total number of background events for the specified activity case is negligible in this region. This is the reason why the limit of 2.303 on the number of excluded signal events is reached, according to the statement made on Feldman-Cousins statistics. For the two measured activity cases, the expected number of background events increases significantly, explaining the degradation of the sensitivity. Hopefully, both regions of interest are highly

Activity ROI	Specified [2.7;3.15] MeV	Measured (w/o ^{214}Bi) [2.75;2.95] MeV	Measured (w/ ^{214}Bi) [2.7;2.9] MeV
$\epsilon_{0\nu}$ (%)	14.7	11.3	14.3
$2\nu\beta\beta$	0.418	0.122	0.418
^{208}Tl	0.0475	0.688	0.699
^{214}Bi	0.0546	0	1.55
^{222}Rn	0.292	0.173	0.287

Table 3.2: Expected number of background events in the $2e$ topology, in the optimised ROI, for the SuperNEMO demonstrator (17.5 kg.y). Three levels of contamination are considered. The selection efficiencies of $0\nu\beta\beta$ events, $\epsilon_{0\nu}$, are also given.

reduced, especially for the case without ^{214}Bi , where the lower bound is increased from 2.7 to 2.75 MeV. As this 50 keV wide energy region is populated with a non-negligible number of background events, this change in E_{\min} usefully reduces the $2\nu\beta\beta$ background contribution, thereby limiting the increase of total expected number of background.

The degradation of the limit on the $0\nu\beta\beta$ half-life with the level of contamination remains acceptable. However, we can try improving the situation by exploring new background rejection techniques. This would be especially useful for the final detector case, where a slight increase in internal contaminations could be highly harmful, all the more so as the upper limit given for ^{214}Bi turns out to be the true contamination level.

3.4.2 Optimisation of event selection

Following the BiPo radiopurity measurements, we wish to implement additional event selections, to reject a higher quantity of background. Most of the double beta experiments are only sensitive to the total electron energy sum. The unique SuperNEMO tracko-calo technology confers the experiment the ability to characterise single particles (individual energies, emission angles...). Based on previous studies [9] [29], *topological cuts*, relying on these additional observables, can be set up. They are especially designed to reject events where the two electrons are not emitted simultaneously, or from the same location on the source foils.

3.4.2.1 The internal probability

Based on time-of-flight (TOF) computation, the internal probability (P_{int}) is derived from the internal χ_{int}^2 (see details in Sec. 2.5.1). In Fig. 3.5 are presented the internal probability spectra for the $0\nu\beta\beta$ signal and all background processes, after the first-order selections. These distributions are normalised to the double beta half-lives, and the nominal activities. Equivalent distributions, but with different ^{214}Bi and ^{208}Tl contamination levels, can be derived for the case of measured activities. The internal probability distributions for the $0\nu\beta\beta$ and $2\nu\beta\beta$ processes follow the expected flat distribution for electrons emitted simultaneously from the source. As internal Bismuth disintegration actually takes place inside the

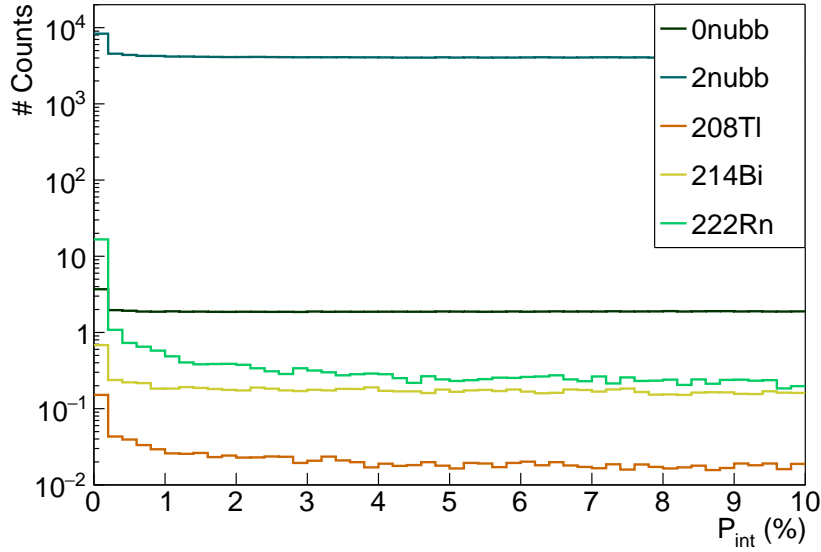


Figure 3.5: Internal probabilities for all processes. First-order cuts have been applied. $\beta\beta$ distributions are normalised to the half-lives, and background processes are normalised to the specified activities.

sources, the ^{214}Bi distribution is also flat. The same could have been assumed for Thallium, however, the distribution is distorted at low internal probabilities. This might be explained by the existence of a metastable excited state ($\tau_{1/2} = 294\text{ps}$) of the daughter nuclei, which would slightly delay the second electron emitted via internal conversion. This feature is addressed in detail in Chap. 4. The Radon, being a non-internal background, presents a large peak at low internal probabilities.

We want to evaluate the influence of a cut-off on the simulations using internal probability as a rejection criterion: simulated events are selected only if their P_{int} value is upper than a given limit. The standard value applied in NEMO-3 analyses was $P_{int} > 4\%$. We wish to establish the most adequate P_{int} selection level for the SuperNEMO demonstrator. To do so, we vary the P_{int} minimal value applied on simulations, and for each we evaluate the limit reached on $T_{1/2}^{0\nu}$ (at a 90 % confidence interval), as well as the optimised ROI. The best internal probability cut-off value to be applied is the one maximising this sensitivity, and is specific for each contamination level.

We depict in Fig. 3.6 a set of four figures that help to better understand this optimisation. We consider two levels of contamination $\sigma_{\beta\beta}$ specified and measured contamination levels (taking the upper limit for ^{214}Bi). We first detail these figures for the case of the specified activities and then explain what we observe for the measured activities.

Specified activities The total expected number of background in the ROI (Fig. 3.8a) is very low, even for $P_{int} > 0\%$, and constantly decreases with P_{int} . Therefore, the number of excluded signal events, $N_{0\nu}^{\text{excl.}}$, is set to its minimum value of 2.303, regardless of the P_{int} level. As a consequence, the ROI bounds are stable (Fig. 3.11a). As the ROI do not influence the selection efficiencies, $\epsilon_{0\nu}$ is only

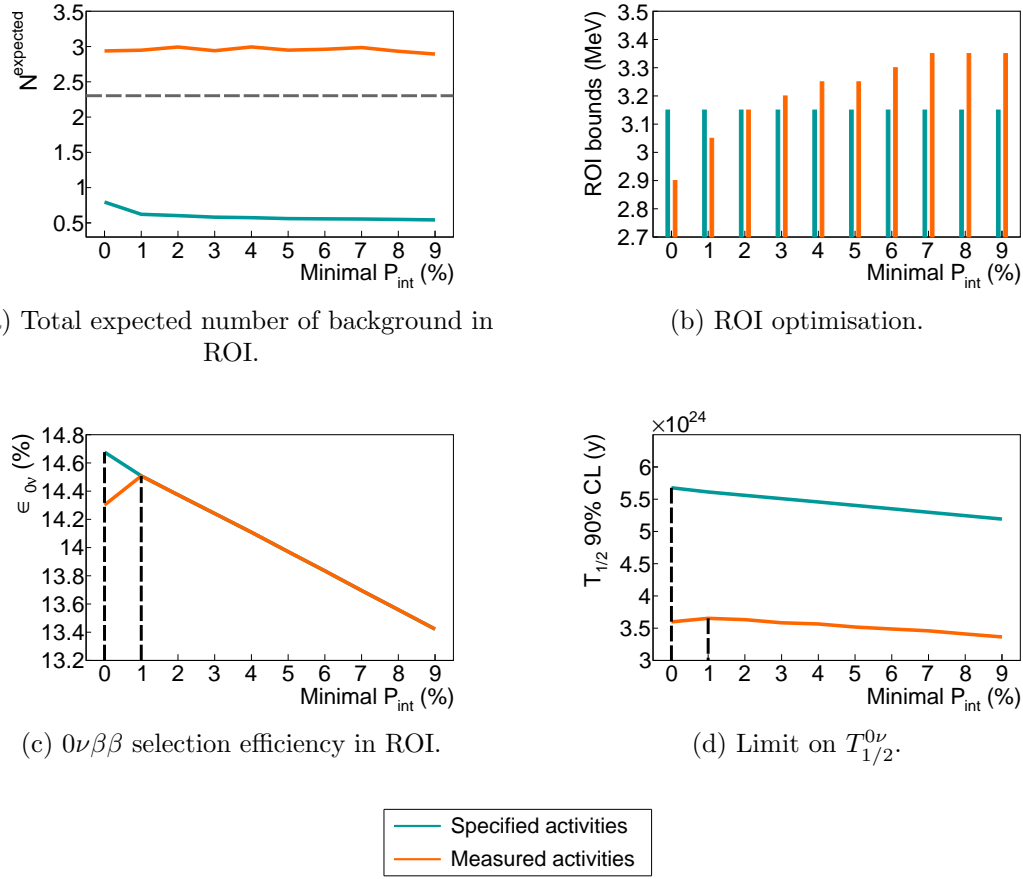


Figure 3.6: Total number of expected background in ROI (a), evolution of the regions of interest (b), $0\nu\beta\beta$ selection efficiency in ROI (c), and limit set on $T_{1/2}^{0\nu}$ at 90% CL (d), as a function of the cut-off applied on internal probability, P_{int} . The ROI is optimised for each P_{int} value. Results are displayed for two contamination levels: the specified (blue) and the measured (orange) activities (taking into account the upper limit provided for ^{214}Bi). An exposure of 17.5 kg.y is considered. Two vertical dashed lines in (c) and (d) display the best P_{int} selections to be applied in order to improve the $T_{1/2}^{0\nu}$ sensitivity of the experiment.

impacted by the P_{int} level applied, and decreases with it (Fig. 3.11b). All these observation allow to understand the evolution of $T_{1/2}^{0\nu}$ (Fig. 3.8d), decreasing with the P_{int} level applied on simulations. The sensitivities displayed for a 0% cut-off on P_{int} of course correspond to the results given in Fig. 3.4.

Measured activities The total number of expected background event is, naturally, higher than for the specifications, and above all is greater than the 2.303 limit. Nevertheless, this level is too low for the P_{int} cut-off to have an impact and the number of expected background remains constant. When the minimal acceptable P_{int} is changed from 0 to 1 %, the ROI upper bound increases from 2.9 to 3.05 MeV. Usually, the variation of this bound does not have such a great impact on the event selection. Nevertheless, in the measured activities case, for a $P_{int} > 0$ % level, the ROI is optimised at the narrow [2.7;2.9] MeV

interval, where the upper bound is located in an energy region still populated by signal (see Fig. 3.4). Therefore, even small variations in this ROI has a great impact on the $0\nu\beta\beta$ selection efficiency, explaining this local increase. We then observe a slight increase of $0\nu\beta\beta$ selection efficiency for the level $P_{int} > 1\%$. For P_{int} selections greater than 1 %, we come back in cases where the upper limit of the ROI no longer has an impact on $\epsilon_{0\nu}$. At this level, only variations of the total number of events, showed in Fig. 3.8a have an impact. As the limit set on $T_{1/2}^{0\nu}$ depends directly on $\epsilon_{0\nu}$, the variations presented in Fig. 3.11b fully explain the results displayed in Fig. 3.8d, presenting the evolution of $T_{1/2}^{0\nu}$ with the internal probability selection level.

The main conclusion is that this rejection criterion has only a limited impact on the improvement of $T_{1/2}^{0\nu}$ sensitivity, because of the very low contamination levels considered. Indeed, paradoxically, the selection on internal probability worth it only if there is enough background events to be rejected, as we can start observing for the measured activities case. Nevertheless, we recommend to keep at least a loose cut-off at $P_{int} > 4\%$ for the specified activities. Indeed, the sensitivity is only slightly degraded, and this would increase the rejection of potential harmful external backgrounds for a more general study.

3.4.2.2 Vertices distance

NEMO-3 analyses also used the distance between the reconstructed vertices on the source foils as a background rejection criterion. As we shown that the additional P_{int} cut-off is poorly adapted for the low activities of Supernemo sources, it is interesting to know if we can improve the results by using this second selection. As discussed in Sec. 3.2, an electron is defined as a reconstructed track inside the wire chamber, with one extremity on a calorimeter block, and another on a source foil. Therefore, the $2e$ topology involves two distinct calorimeter hits, two reconstructed tracks, and two foil vertices. Thanks to the trajectory fitting algorithm, we have access to the (Y, Z) coordinates of the latter, and by extension, to the distance between them. In the previous studies, the choice was made to look at the effect of this selection, separately on the Y (perpendicular to the wires) and Z (parallel to the wires) directions. We choose to follow the same approach, and we give the results for a cut along the Z axis, but the conclusions would remain valid for the Y direction. Fig. 3.7 shows the distributions of the absolute value of the distance between foil vertices for each process studied. We would use this information in order to maximise the double β decays to be selected, while rejecting natural isotope disintegrations.

In the same way as the previous paragraph, Fig. 3.8 displays all informations leading to the maximisation of $T_{1/2}^{0\nu}$, allowing to study the impact of the vertices distance cut-off on the final sensitivity. Overall, these figures show us that too strict cut-off on the distance between vertices would lead to a decrease in sensitivity. Because of the variations of the $0\nu\beta\beta$ selection efficiency and the total number of background events, the $T_{1/2}^{0\nu}$ distributions reaches a plateau, corresponding to the sensitivities achieved with the first-order cuts and optimised P_{int} . In practice, as it is done for P_{int} , a selection on vertex distance will always be applied, even if it is very loose, as such a cut-off could be useful for rejecting unexpected background

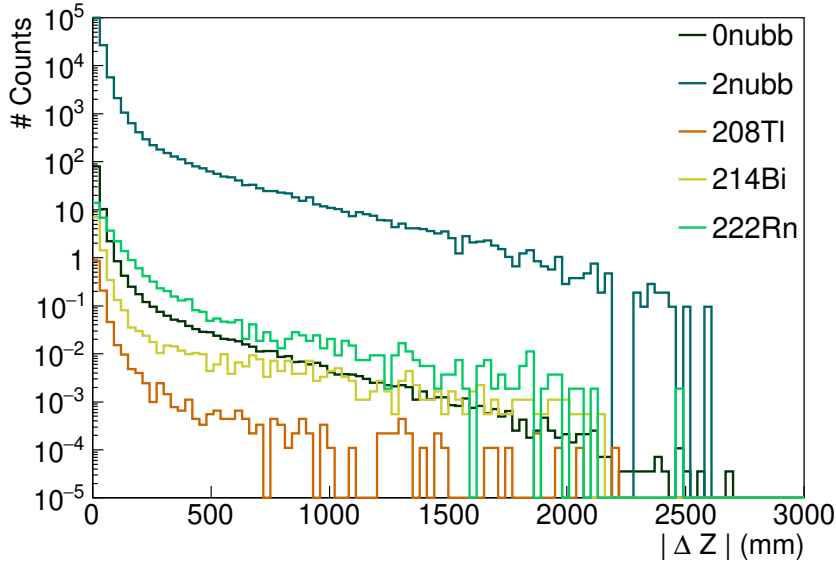


Figure 3.7: Distance along the Z direction between the vertices of the 2 reconstructed electrons, for each process considered. The $2\nu\beta\beta$ spectrum is normalised to $T_{1/2}^{2\nu} = 9.39 \times 10^{19}$ y, and ^{208}Tl , ^{214}Bi and ^{222}Rn backgrounds are normalised to the nominal activities. The amplitude of the $0\nu\beta\beta$ is arbitrarily set at the limit obtained with NEMO-3. No energy cut is applied.

(coincidence between independent events, for instance). We recommend to apply a loose cut-off level at $|\Delta Z| < 80$ mm, which does not degrade significantly the sensitivity. The same conclusions apply to the $|\Delta Y|$ cut-off.

The idea of having implemented these two selections (on the internal probability and on the distance between vertices) comes from a previous NEMO-3 analysis on the background rejection. For the SuperNEMO demonstrator case, the levels of contaminations we are dealing with is remarkably low for most of the topological cut-offs to be worth applying. However, in practice, applying loose topological selections on the data remains necessary, especially to reject external background events. The minimal cut-off level to be applied is $P_{int} > 4\%$ and $|\Delta Z| < 80$ mm (samely for $|\Delta Y|$), and can be optimised by taking into account the sources activity.

For future studies, it is useful to give the efficiencies of these loose selections, for the signal and for each background considered (Tab. 3.3a), as well as the expected number of background in the ROI (Tab. 3.3b). As detailed, regions of interest are optimised for each selection. The selection efficiencies show topological cuts have a huge impact on Radon selection, as they are especially designed to reject non-internal events. They are also efficient in rejecting Thallium internal events, because of the existence of a metastable excited state, described earlier. A special technique to reject efficiently ^{208}Tl background is also addressed in Chapter 4.

After the topological cut-off optimisation, the SuperNEMO demonstrator would reach a sensitivity of $T_{1/2}^{0\nu} > 5.4 \times 10^{24}$ y if specified activities are reached,

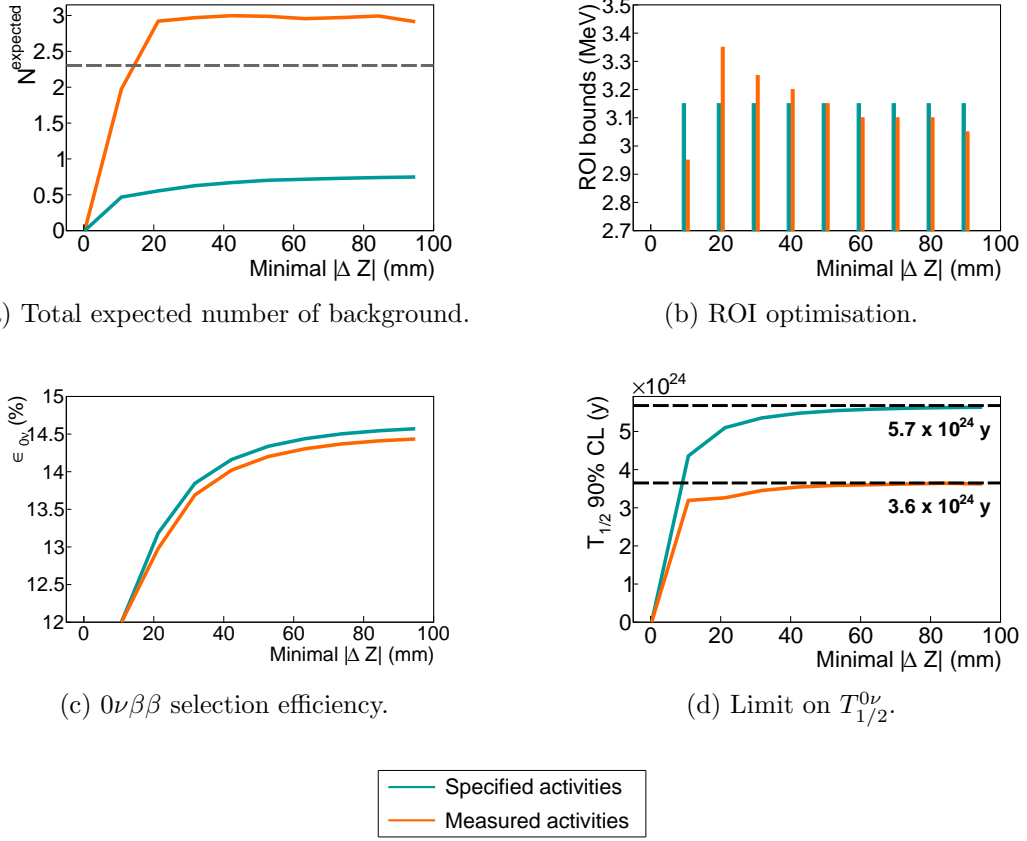


Figure 3.8: Total number of expected background in ROI (a), evolution of the regions of interest (b), $0\nu\beta\beta$ selection efficiency in ROI (c), and limit set on $T_{1/2}^{0\nu}$ at 90% CL (d), as a function of the cut-off applied on distance between vertices, $|\Delta Z|$. The ROI is optimised for each $|\Delta Z|$ value. Results are displayed for two contamination levels: the specified (teal) and the measured (orange) activities (taking into account the upper limit provided for ^{214}Bi). An exposure of 17.5 kg.y is considered.

corresponding to the effective neutrino mass range $\langle m_{\beta\beta} \rangle < [0.25 - 0.48]$ eV. For the measured activities, supposing ^{214}Bi activity reaches the measured upper limit, $T_{1/2}^{0\nu} > 3.6 \times 10^{24}$ y and $\langle m_{\beta\beta} \rangle < [0.31 - 0.59]$ eV.

In the following we review the influence of the 25 Gauss magnetic field inside the detector on the sensitivity reachable by the SuperNEMO demonstrator.

3.5 Impact of the magnetic field on the sensitivity

The SuperNEMO demonstrator was originally designed with a copper coil, similarly to NEMO-3, delivering a magnetic field inside the tracker volume. This 25 Gauss magnetic field is high enough to bend the trajectory of the few MeV electrons and positrons of interest for SuperNEMO, without too strongly preventing them from reaching the calorimeter. In practice, this magnetic field

3.5. Impact of the magnetic field on the sensitivity

Cut-off	First-order cuts (%)	Internal probability (%) $P_{int} > 4\%$	Vertex distance (%) $ \Delta Z < 80 \text{ mm}$
$0\nu\beta\beta$	26.9	25.3	24.7
$2\nu\beta\beta$	9.15	8.56	8.21
^{208}Tl	0.106	0.0889	0.0846
^{214}Bi	0.168	0.151	0.144
^{222}Rn	0.0177	7.91×10^{-3}	5.34×10^{-3}

(a) Selection efficiencies (number of selected $2e$ topologies compared with the total number of simulated decays), for the three levels of selection (first-order, P_{int} and vertex distance), in the full energy range.

Activity	Specified		Measured (w/ ^{214}Bi)	
Cut-off ROI (MeV)	$P_{int} > 4 \%$ [2.7;3.15]	$ \Delta Z < 80 \text{ mm}$ [2.7;3.15]	$P_{int} > 4 \%$ [2.7;3.25]	$ \Delta Z < 80 \text{ mm}$ [2.7;3.3]
$\epsilon_{0\nu} (\%)$	14.1	13.9	14.1	13.9
$2\nu\beta\beta$	0.392	0.383	0.392	0.383
^{208}Tl	0.0338	0.0323	1.08	1.09
^{214}Bi	0.0491	0.0491	1.42	1.42
^{222}Rn	0.115	0.0782	0.115	0.0782

(b) Expected number of background events in the optimised ROI, for successive application of topological selections. The selection efficiency of $0\nu\beta\beta$ events in the ROI, $\epsilon_{0\nu}$, is also given. Specified and measured activities (taking into account the upper limit for ^{214}Bi contamination) are considered. The SuperNEMO demonstrator exposure of 17.5 kg.y is taken.

Table 3.3: The selection efficiencies and expected number of background events for the topological selections.

is mainly used to identify and reject the electron-positron pairs created by high energy γ 's, themselves emitted after a neutron capture. However, as explained in sub-section 3.1.3, we choose to not consider the contribution of this external background for this study's background model. We therefore focus on evaluating the influence of the presence of the magnetic field on the rejection of natural isotopes contaminating the source foils and wire chamber.

3.5.1 Simulations of the magnetic field inside the demonstrator and reconstructed track fit

In order to study the influence of the magnetic field on the demonstrator sensitivity to the $0\nu\beta\beta$ decay, the simulations and reconstructions of signal and backgrounds have been performed in two different conditions.

- Simulations with a uniform 25 Gauss magnetic field (following recommendations [9]). Results about the final sensitivity achieved in this condition have already been presented earlier in this chapter. The possible variations of the field intensity, mainly due to the calorimeter magnetic shields, are not taken into account for these simulations. This will be discussed in sub-section 3.5.4.

- Simulations where the magnetic field is turned off.

Each magnetic field condition has the same number of simulated events, as summed up in Tab. 3.1.

Depending on the case under consideration, the charged particles do not have the same trajectory curvature. In the first uniform on-field case, they are bended. The track fit algorithm then performs two distincts trajectory fittings: one with an helix and one with a line. The most accurate fit is chosen and provides information on the charge of the detected particle. In the second off-field case, the fitting algorithm is modified to match line trajectories.

3.5.2 Impact of the magnetic field on signal and background selections

Among first-order event selection criteria considered in Sec. 3.2, the one on the trajectory curvature is of primary importance with regard to the influence of the magnetic field on the final sensitivity. Indeed, when the magnetic field is switched on, the charged particles of few MeV (as electrons and positrons) have curved trajectories. A particle is then identified as an electron when the trajectory fitting results in a negative curvature. When the magnetic field is switched off, the trajectory of the charged particles takes place in a straight line⁴. This last selection criterion on the track curvature is then no longer applied.

Consequently, the number of identified $2e$ topologies selected by the first-order cuts is increased for the off-field case. To illustrate this effect, we give in Tab. 3.4 the selection efficiencies of signal and background in the total energy range $[0;4]$ MeV, for the two cases of magnetic field. The field being turned-off,

Field	On	Off
$0\nu\beta\beta$	26.9	31.4
$2\nu\beta\beta$	9.16	10.6
^{208}Tl	0.106	0.169
^{214}Bi	0.168	0.252
^{222}Rn	0.0177	0.0924



Table 3.4: Selection efficiencies in the full energy range $[0;4]$ MeV, for on and off-field cases. First-order cut-offs have been applied.

electrons and positrons are no more discriminated, enhancing the number of 2 topologies selected. However only variations of $\epsilon_{0\nu}$ in the ROI, between on-field and off-field cases, are the source of modifications on the final sensitivity. We present in Tab. 3.5 the selection efficiencies of the signal and backgrounds, in the ROI, for the two field cases. The selection efficiency of $\beta\beta$ decays are unfavoured, for the off-field case, by the lower bound of the ROI. The slight variation of the ROI upper bound have a measurable impact on the expected number of ^{208}Tl events, as this background has a contribution at high energies. The increase of ^{222}Rn events,

⁴In saying this, we do not take into account possible deviations in the trajectory of the particles, due in particular to multiple scattering in the tracker.

Field	On [2.7;3.15] MeV	Off [2.75;3.2] MeV
$\epsilon_{0\nu}$ (%)	14.7	12.4
$2\nu\beta\beta$	0.418	0.0353
^{208}Tl	0.0475	0.0600
^{214}Bi	0.0546	0.0452
^{222}Rn	0.292	0.553

Table 3.5: Expected number of background events in the optimised ROI, for the SuperNEMO demonstrator (17.5 kg.y), for specified activities. The selection efficiency of $0\nu\beta\beta$ events, $\epsilon_{0\nu}$, is also given. The two on- and off-field cases are compared. First-order cut-offs have been applied.

despite the ROI lower bound variation, is directly explained by [besoin d'aide ici]. As expected, these observations result in a decrease in sensitivity when the field is switched off, giving

$$T_{1/2}^{0\nu} > 4.8 \times 10^{24} \text{ y} \quad (90\% \text{CL}) \text{ (off-field)}. \quad (3.10)$$

As concluded in Sec. 3.4, topological selections are especially efficient in rejecting the Radon background. Therefore, the application of these additionnal cut-offs, for the off-field case, could be interesting, in order to increase the sensitivity. Following the work presented in the previous section, we optimise these selections for the particular off-field case, both for the specified and measured contamination levels⁵. Fig. 3.9 summarises the results obtained in sensitivity before and after application of these topological cut-offs. The left part of the panel gives information on the evolution of sensitivity, when only the first-order cut-offs are applied. We come back to the conclusions given above: when the magnetic field is switched-off, we lose sensitivity, regardless of the level of contamination considered. On the right side of the figure, we present the results when the topological cuts are applied. For the on-field case, the addition of these selections have almost no effect on the sensitivity, as concluded in sub-section 3.4.2. However, as predicted, we are beginning to see the usefulness of these selections in the off-field case, as a higher number of ^{208}Tl and ^{222}Rn events passed the first-order selections. For instance, for the specification case, $T_{1/2}^{0\nu}$ goes from $4.8 \times 10^{24} \text{ y}$ to $6.1 \times 10^{24} \text{ y}$, an improvement of $\sim 30\%$. In Tab. 3.6 are presented the expected number of background events in the ROI for the off-field condition. The influence of topological cut-offs is presented, for the specified and measured activities (taking into account the upper limit for the ^{214}Bi contamination). Topological cut-off application allow to reject mainly ^{222}Rn background. Although the expected number of $2\nu\beta\beta$ events increases because of the ROI lower bound, it is compensated by the gain in $0\nu\beta\beta$ selection efficiency. Finally, even if the absence of the magnetic field has the effect of reducing the sensitivity to the $0\nu\beta\beta$ decay, topological cuts allow this effect to be compensated for, making it possible to reach higher values of $T_{1/2}^{0\nu}$.

⁵As done in sub-section 3.4.2, for the Bismuth measured contamination, we consider here the upper limit where $\mathcal{A}^{\text{Bi}} = 290 \text{ } \mu\text{Bq/kg}$.

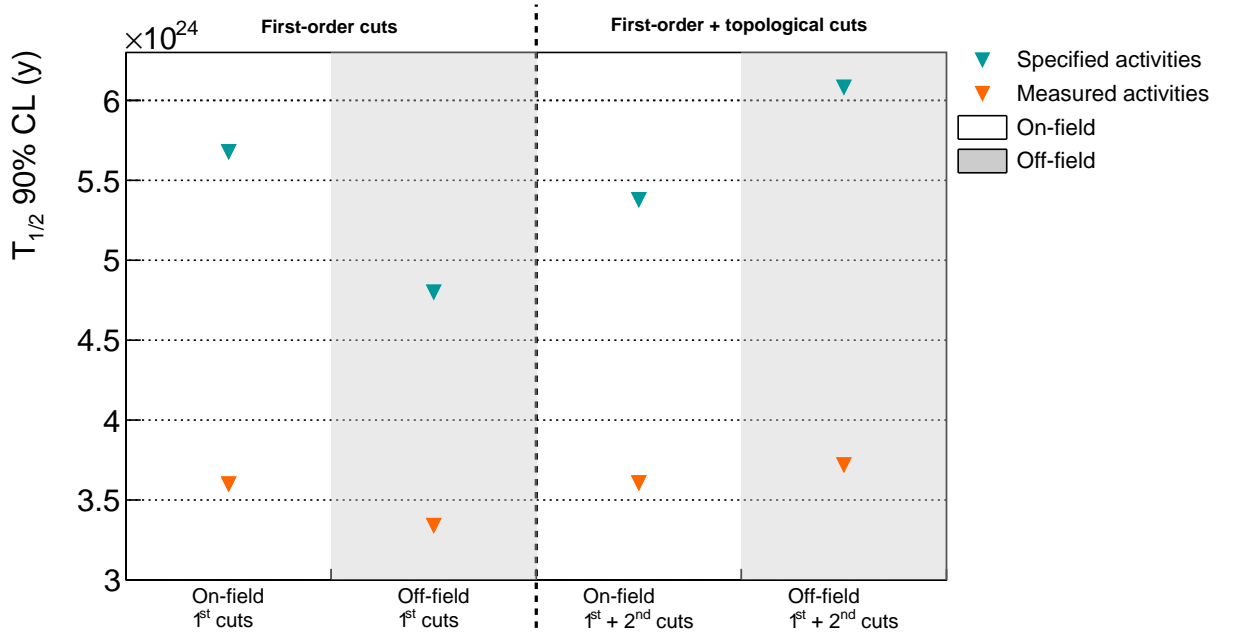


Figure 3.9: $T_{1/2}^{0\nu}$ (90% CL) considering various conditions: on- and off-field (white and gray stripes), first-order and addition of topological cut-offs (left/right parts of the panel), specified and measured activities (blue and orange triangle markers). The measured activities are $\mathcal{A}^{\text{Tl}} = 54 \mu\text{Bq/kg}$, $\mathcal{A}^{\text{Bi}} = 290 \mu\text{Bq/kg}$ and $\mathcal{A}^{\text{Rn}} = 0.15 \text{ mBq/m}^3$.

Activity	Specified		Measured (w/ ^{214}Bi)	
Cut-off ROI (MeV)	First-order [2.75;3.2]	Topological [2.7;3.2]	First-order [2.65;2.9]	Topological [2.7;2.9]
$\epsilon_{0\nu}$ (%)	12.4	15.7	19.1	14.8
$2\nu\beta\beta$	0.0353	0.453	1.56	0.440
^{208}Tl	0.0600	0.0506	1.01	0.613
^{214}Bi	0.0452	0.0706	2.94	1.84
^{222}Rn	0.553	0.0894	1.42	0.0689

Table 3.6: Expected number of background events in the optimised ROI, with off-field condition. The selection efficiency of $0\nu\beta\beta$ events in the ROI, $\epsilon_{0\nu}$, is also given. Exposure of the SuperNEMO demonstrator (17.5 kg.y). Specified and measured (with ^{214}Bi) activities are considered. Topological cut-offs are optimised: $P_{\text{int}} > 1\%$ and $|\Delta Z| < 80\text{mm}$ (specified activities), $P_{\text{int}} > 5\%$ and $|\Delta Z| < 80\text{mm}$ (measured activities)

3.5.3 Influence of the magnetic field on optical modules and reconstruction efficiency

In the previous sub-section, a comparative study has been lead to evaluate the influence of the presence of a magnetic field on the event selection, and thus on the final sensitivity. However, as things stand now, some features of the demonstrator are not yet implemented in the simulation software, and could have

a great impact on the results presented above. In particular, studies have been lead by the collaboration to evaluate the influence a 25 Gauss magnetic field on the optical modules, as well as on the event reconstruction [9][10].

SuperNEMO PMTs are protected from the external magnetic field by individual, cylindrical, iron shields. Unfortunately, the latter do not perfectly protect the PMTs, and a residual magnetic field is measured inside the shieldings, leading to losses in charge collected by PMTs close to 8%. This study also revealed the energy resolution would be worsened with a relative decrease of 3% of the initial value of 8% at 1 MeV. Moreover, the PMTs shieldings could themselves severely impact the shape of the field lines, as well as its intensity. In fact, with a 25 Gauss magnetic field generated by the copper coil, the magnetic shields are responsible for the field strength decreasing, and barely 10 G is expected near the source foils. Worse, the magnetic field strength decreases very quickly as we get closer to the calorimeter walls, where nearly 0 G could be expected. The reconstruction efficiency could therefore be greatly impacted: the magnetic field intensity varying from the source foils to the calorimeter wall, electrons trajectory curvatures are unconstant, and the track-fitting algorithm is less performing. An uncorrect description of the distribution of the magnetic field would more strongly impact low-energy electrons.

In the light of these conclusions, it could be interesting to study the evolution of the sensitivity, considering field simulations with more realistic variations inside the detector.

3.5.4 Simulations with a non-uniform magnetic field

Simulations with a 25 Gauss *mapped* magnetic field have been performed, taking into account more realistic variations of the field inside the detector [30]. In this condition, the fitting algorithm follows the same steps as for on-field: an helix and linear fit are performed for each simulated event, and the most accurate is selected. Unfortunately, Radon isotope decays could not be simulated with this magnetic field configuration. Indeed, as it is present in the entire wire chamber, simulations would have required too many additional storing resources. Thus, final conclusions on the sensitivity can't be given. However, it is possible to assess the selection efficiencies of the different processes, and then get an idea of the influence of realistic variations of the field on the final results. Tab. 3.7 compares the selection efficiencies, for the three field cases (uniform on-field, mapped field and off-field), in the total energy range [0;4] MeV. The mapped field case has lower selection efficiencies, compared with uniform field simulations. As announced in the previous sub-section, the magnetic shields distort the field intensity accross the detector. Therefore, the fitting algorithm is less performant in identifying particles with a negative curvature inside the tracker, hence the number of selected $2e$ topologies is decreased.

Tab. 3.8 presents the expected number of background events in the energy range [2.7;3.2] MeV, for simulations using the realistic mapped field. As expected, the $0\nu\beta\beta$ selection efficiency is drastically decreased compared with the on-field case, as well as the expected number of background events.

Field P_{int}	On $P_{int} > 4\%$	Off $P_{int} > 1\%$	Mapped $P_{int} > 4\%$
$0\nu\beta\beta$	24.7	29.3	19.1
$2\nu\beta\beta$	8.21	9.93	6.39
^{208}Tl	0.0846	0.140	0.0774
^{214}Bi	0.144	0.211	0.125

Table 3.7: Signal and background selection efficiencies of on-field, off-field and mapped-field cases, in the energy range [0;4] MeV. The first-order and optimised topological cut-offs have been applied. For all field conditions, the selection $|\Delta Z| < 80$ mm have been applied.

	Mapped field
$\epsilon_{0\nu}$ (%)	10.4
$2\nu\beta\beta$	0.245
^{208}Tl	0.0279
^{214}Bi	0.0535

Table 3.8: Expected number of background events in the optimised energy range [2.7;3.2] MeV, for mapped field simulations. The $2\nu\beta\beta$ half-life is taken as $T_{1/2}^{2\nu} = 9.39 \times 10^{19}$ y, and the nominal background activities are considered. We assume a 17.5 kg.y exposure. First-order and optimised topological cuts have been applied ($P_{int} > 4\%$ and $|\Delta Z| < 80$ mm).

Even if Radon simulation with such field conditions are not available, it is interesting to provide an order of magnitude of the $T_{1/2}^{0\nu}$ limit set with these realistic variations of the field. To do so, we extrapolate the expected number of Radon events in the [2.7;3.2] MeV energy range, from the ^{214}Bi one. Indeed, we postulate the ratio between these two numbers is a constant, and the on-field simulations give $N_{\text{Bi}}/N_{\text{Rn}} \sim 5$. Taking this into consideration, a limit of $T_{1/2}^{0\nu} > 4 \times 10^{24}$ y (90 % CL) would be reached with the demonstrator, a ~ 30 % decrease compared with the non-realistic uniform case.

3.6 Searching for the Neodymium-150 $0\nu\beta\beta$ decay

This study was conducted jointly with the PhD student Axel Pin, from CENBG [31]. Although we both worked on the whole of the analysis, I presented in detail, in the previous sections, the results regarding the influence of the magnetic field. Meanwhile, Axel Pin presents the possibility of changing the Selenium material by other $\beta\beta$ isotopes. Indeed, on the model of the NEMO-3 detector, which housed, among others, 6.914 kg of ^{100}Mo and 0.932 kg of ^{82}Se , the SuperNEMO detector possesses the technical possibility of exchanging the source material and study several $\beta\beta$ isotopes. Notably, in the case SuperNEMO demonstrates the feasibility of a large-scale tracko-calorimeter experiment, it would be natural to evaluate the sensitivity of SuperNEMO to the $0\nu\beta\beta$ decay of other

isotopes than ^{82}Se .

3.6.1 Searching for the $0\nu\beta\beta$ of other isotopes

One of the distinctive features of NEMO detectors is the gas chamber, designed to track charged particles. Unluckily, this advantage is also a great inconvenience when it comes to Radon contamination. Indeed, Radon enters by diffusion or emanates from the detector materials. It is then interesting to consider $\beta\beta$ candidates with an energy transition value above the $Q_\beta = 3.27$ MeV of Radon. Another useful criterion is the natural isotopic abundance: typically, considering only isotopic abundances greater than 2% is a reliable basis when selecting potential $\beta\beta$ emitters. Two nuclei satisfy these two criteria: ^{96}Zr and ^{150}Nd (with respective $Q_{\beta\beta}$ values of 3.35 and 3.36 MeV, and respective isotopic abundances of 2.8 and 5.6 % [32]). As the ^{150}Nd isotope has the highest $Q_{\beta\beta}$ value, the current section focuses on evaluating the SuperNEMO sensitivity to the $0\nu\beta\beta$ decay of this isotope, supposing we have several kg at our disposal.

3.6.2 Sensitivity to the $0\nu\beta\beta$ of ^{150}Nd

Until recently, Neodymium was not enrichable in large quantities by centrifugation. Recent developments have resulted in the production of several grams of enriched Neodymium, making this $\beta\beta$ isotope interesting for the search of $0\nu\beta\beta$. Thanks to that, NEMO-3 had available 36.6 g of ^{150}Nd which were recovered by the collaboration, for a possible reuse for SuperNEMO. The best limit for the search for neutrinoless double β decay of ^{150}Nd was reached by the NEMO-3 detector with 5.25 years of data acquisition. The detector achieved $T_{1/2}^{0\nu} > 2.0 \times 10^{23}$ y (90 % CL), corresponding to an upper limit on the effective neutrino mass of $\langle m_{\beta\beta} \rangle < [1.6 - 5.3]$ eV. The collaboration also measured the $2\nu\beta\beta$ half-life, with $T_{1/2}^{2\nu} = [9.34 \pm 0.22 \text{ (stat.)} \pm_{0.60}^{0.62} \text{ (syst.)}] \times 10^{18}$ y [34].

We wish to determine the limit on the $0\nu\beta\beta$ of the ^{150}Nd that could be reached with the SuperNEMO demonstrator, with an exposure of 17.5 kg.y. We lead this study considering the activities specified for the ^{82}Se sources are reached. We use simulations with the 25 Gauss uniform magnetic field. Fig. 3.10 depicts the normalised energy distributions for the $2e$ topologies selected after application of first-order and topological selections. Signal and background selection efficiencies for ^{150}Nd sources, in the total energy range, are given in Tab. 3.9. In this energy

Material	Selenium	Neodymium
$0\nu\beta\beta$	25.8	25.5
$2\nu\beta\beta$	8.21	8.11
^{208}Tl	0.0846	0.0749
^{214}Bi	0.144	0.138
^{222}Rn	5.34×10^{-3}	5.34×10^{-3}

Table 3.9: Selection efficiencies in the full energy range [0;4] MeV, for ^{82}Se and ^{150}Nd sources. First-order and optimised topological cuts have been applied.

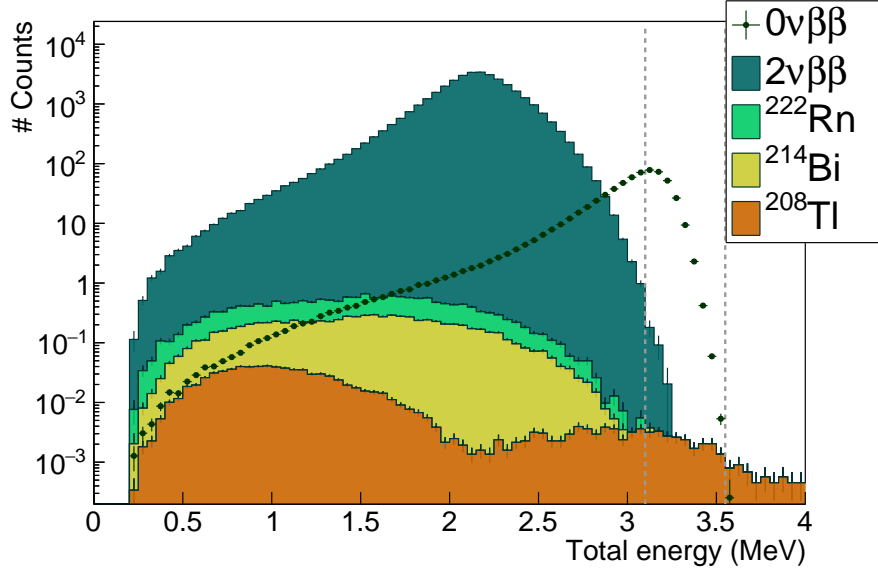


Figure 3.10: Total energy spectra for the $0\nu\beta\beta$ signal and main backgrounds, for ^{150}Nd sources. The $2\nu\beta\beta$ spectrum is normalised to $T_{1/2}^{2\nu} = 9.34 \times 10^{18}$ y, and ^{208}Tl , ^{214}Bi and ^{222}Rn backgrounds are normalised to the nominal activities. The amplitude of the $0\nu\beta\beta$ is arbitrarily set at the limit obtained with NEMO-3 $T_{1/2}^{0\nu} = 2.0 \times 10^{23}$ y. We assume a 17.5 kg.y exposure. First-order and optimised topological cuts have been applied. The ROI of [3.1;3.55] MeV is depicted by two vertical dashed lines.

range, the background is dominated by the $2\nu\beta\beta$ decay. The selection efficiencies of backgrounds are lower for ^{150}Nd sources than for ^{82}Se sources. This is caused by the higher number of protons in the Neodymium nucleus which induces a stronger Coulombian effect. Indeed, internal electrons are more likely to interact with the source material, which is particularly true for low energy electrons. We used the same Radon simulations as for ^{82}Se sources, neglecting possible effects due to a higher proton number.

In Tab. 3.10 we give the expected number of background events in the optimised ROI [3.1;3.55] MeV. The selection efficiency of the $0\nu\beta\beta$ decay in this energy range

Material ROI	Selenium [2.7;3.15] MeV	Neodymium [3.1;3.55] MeV
$\epsilon_{0\nu}$ (%)	14.4	10.3
$2\nu\beta\beta$	0.39	0.28
^{208}Tl	0.044	0.029
^{214}Bi	0.053	5.6×10^{-4}
^{222}Rn	0.20	0.0

Table 3.10: Expected number of background events in the optimised regions of interest, for ^{82}Se and ^{150}Nd sources. The $2\nu\beta\beta$ half-life taken as $T_{1/2}^{2\nu} = 9.34 \times 10^{18}$ y, and the nominal background activities are considered. We assume a 17.5 kg.y exposure. First-order and optimised topological cuts have been applied.

is also given. Although the $2\nu\beta\beta$ half-life of the ^{150}Nd is lower than that of the ^{82}Se , the number of $2\nu\beta\beta$ events in the ROI remains low. Indeed, thanks to the Coulombian effects described above, this process has a limited contribution at high energy. The high energy of transition $Q_{\beta\beta} = 3.36$ MeV of ^{150}Nd implies that the contributions of ^{214}Bi and ^{222}Rn are very small, or even zero. The $2\nu\beta\beta$ and ^{208}Tl events are therefore the major contributors to the background. Consequently, if the choice of changing the source material with ^{150}Nd isotope was made, it would be conceivable to release the specifications on ^{214}Bi and ^{222}Rn backgrounds.

The SuperNEMO demonstrator, with 7 kg of ^{150}Nd and 2.5 years of data acquisition, would achieve a $T_{1/2}^{0\nu} > 2.2 \times 10^{24}$ y sensitivity, one order of magnitude higher than the best limit ever reached. The corresponding limit on the effective neutrino mass is $\langle m_{\beta\beta} \rangle = [0.15 - 0.50]$ eV. This is a better result than for ^{82}Se sources, as the ^{150}Nd has a more favourable space factor.

3.7 The final detector sensitivity

The ultimate goal of the SuperNEMO demonstrator is to show that the NEMO technology is scalable to probe unprecedented half-life on the $0\nu\beta\beta$ decay. The final detector would consist in building 20 modules similar to the demonstrator. In this context, we estimate the final detector sensitivity to the $0\nu\beta\beta$ decay.

We suppose the specified activities of $\mathcal{A}^{\text{Tl}} = 2$ $\mu\text{Bq/kg}$, $\mathcal{A}^{\text{Bi}} = 10$ $\mu\text{Bq/kg}$ and $\mathcal{A}^{\text{Rn}} = 0.15$ mBq/m³ are reached. The simulations with an uniform magnetic field are used.

Tab. 3.11 shows the number of expected events in the optimised ROI for first-order and topological cut-offs. The total expected number of background events

Cut ROI	First-order [2.75;2.95] MeV	Topological [2.75;3.1] MeV
$\epsilon_{0\nu}$ (%)	11.3	10.7
$2\nu\beta\beta$	3.48	3.36
^{208}Tl	0.728	0.756
^{214}Bi	0.945	0.835
^{222}Rn	6.93	2.16

Table 3.11: Expected number of background events in optimised energy ranges for the SuperNEMO final detector (500 kg.y exposure). The $0\nu\beta\beta$ selection efficiency is also given. The $2\nu\beta\beta$ half-life is taken as $T_{1/2}^{2\nu} = 9.39 \times 10^{19}$ y, and the specified background activities are considered. The topological selections have been optimised: $P_{int} > 4\%$ and $|\Delta Z| < 80$ mm.

is high enough for the optimised cut-offs to be worth it, with $P_{int} > 4\%$ and $|\Delta Z| < 80$ mm (samely for $|\Delta Y|$). They allow primarily to reduce the Radon background by a factor 3. Due to the optimisation of the ROI, especially to the raising of the upper bound, the ^{208}Tl background is a little increased, without important consequences, as the $2\nu\beta\beta$ and ^{222}Rn dominate the total number of background in this energy range.

With an exposure of 500 kg.y, the SuperNEMO final detector should reach a sensitivity of $T_{1/2}^{0\nu} > 5.4 \times 10^{25}$ y, with ^{82}Se sources, corresponding to $\langle m_{\beta\beta} \rangle = [0.079 - 0.15]$ eV. By comparison, with the same exposure and background specifications but with ^{150}Nd sources, the final detector would achieve a sensitivity of $T_{1/2}^{0\nu} > 2.2 \times 10^{25}$ y, in the [3.1;3.75] MeV ROI, corresponding to $\langle m_{\beta\beta} \rangle = [0.046 - 0.15]$ eV.

3.8 Conclusion

Latest measurements of source activities show that the specified background level for Thallium isotope is not reached, although it is improved in average by a factor 2, compared to NEMO-3. An upper limit is given for the internal Bismuth isotope activity, which will be precisely measured by the SuperNEMO demonstrator when data acquisition will begin. C-sections measurements with a concentration line showed the Radon targeted activity is reached for the demonstrator, with an air flow rate of 2 m³/h inside the chamber. Topological selections, designed to reject non-internal and non-simultaneous 2e events, have been optimised, and allowed to reduce the Radon background by a factor 3 for the final demonstrator. Assuming the target background activities are reached, the SuperNEMO demonstrator, running for two and half years with 7 kg of ^{82}Se , would be able to set a limit on the $0\nu\beta\beta$ process $T_{1/2}^{0\nu} > 5.4 \times 10^{24}$ years, translating into a limit on the neutrino effective mass $\langle m_{\beta\beta} \rangle < [0.25 - 0.48]$ eV⁶. Taking into account the measured activities (with 290 $\mu\text{Bq/kg}$ of ^{214}Bi), the limit on $T_{1/2}^{0\nu}$ would be decreased by a factor 33% with $T_{1/2}^{0\nu} > 3.6 \times 10^{24}$ years ($\langle m_{\beta\beta} \rangle < [0.31 - 0.59]$ eV). This limit could be enhanced by using a multivariate analysis, similarly to what is done in other double beta decay experiments, taking advantage of the several topological variables offered by SuperNEMO.

Recent studies have shown that the 25 Gauss magnetic field would be distorted by detector materials, especially the calorimeter magnetic shields. In this context, we studied the influence of this field on the demonstrator sensitivity. Switching-off the field would enhance the expected number of 2e topologies, especially for background processes, and decrease the sensitivity. This effect is compensated by applying optimised topological cut-offs which are useful with such a level of background. Finally, without magnetic field, the SuperNEMO demonstrator would set a limit on the sensitivity of $T_{1/2}^{0\nu} > 6.1 \times 10^{24}$ years ($\langle m_{\beta\beta} \rangle < [0.24 - 0.46]$ eV), taking into account the specified activities, a 13% increase on $T_{1/2}^{0\nu}$ compared with the on-field case. With the measured activities, $T_{1/2}^{0\nu} > 3.7 \times 10^{24}$ years ($\langle m_{\beta\beta} \rangle < [0.30 - 0.58]$ eV), an improvement of 3% compared with the on-field case. Simulations with a mapped field shown that the signal and background selection efficiencies would be degraded by a non-uniform, more realistic magnetic field.

Like its predecessor, the SuperNEMO demonstrator was designed to study several isotopes, such as the ^{150}Nd . Assuming the target background activities

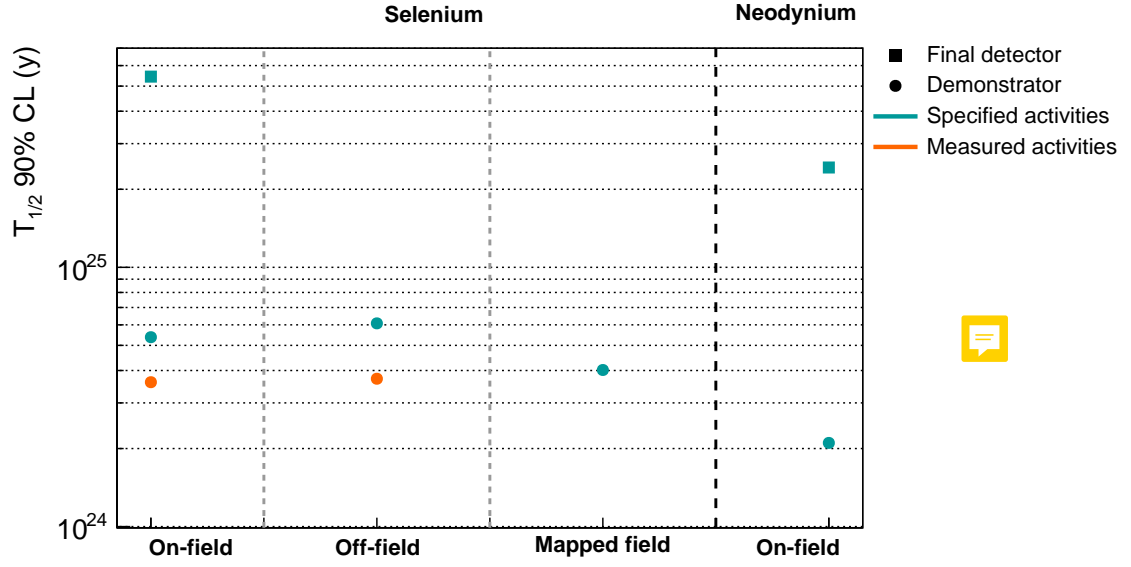
⁶The real mass of isotope is 6.23 kg, then to achieve a 17.5 kg.y exposure, the demonstrator should run a little more than two years and a half.

are reached for ^{150}Nd sources, the SuperNEMO demonstrator would achieve a $T_{1/2}^{0\nu} > 2.2 \times 10^{24}$ years ($\langle m_{\beta\beta} \rangle < [0.15 - 0.51]$ eV).

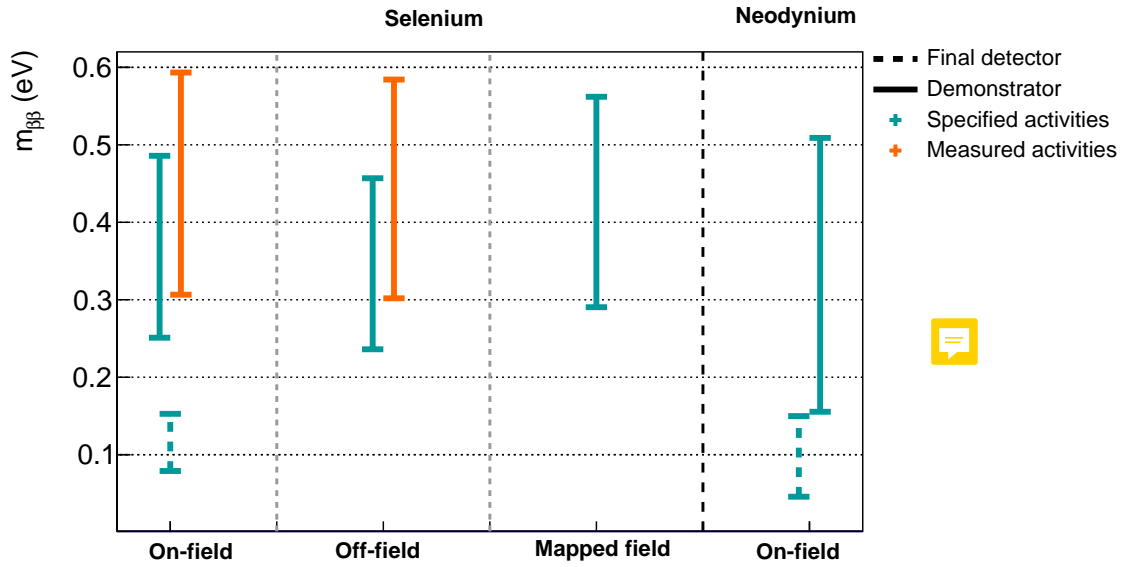
Finally, assuming we reach the target background levels, the SuperNEMO final detector would achieve an unprecedented limit of $T_{1/2}^{0\nu} > 5.4 \times 10^{25}$ years for ^{82}Se sources, corresponding to $\langle m_{\beta\beta} \rangle = [0.079 - 0.15]$ eV. For ^{150}Nd sources, the half-life $T_{1/2}^{0\nu} > 2.4 \times 10^{25}$ years would be reached. This corresponds to $\langle m_{\beta\beta} \rangle = [0.046 - 0.15]$ eV, better than for ^{82}Se sources, thanks to its higher $G^{0\nu}$ factor.

To go further in this study, the SuperNEMO collaboration would study the influence on the sensitivity of external backgrounds, coming from detector materials as well as the laboratory. Also, more realistic performances of the detector, as well as field variations have to be implemented in the software for the simulations to reproduce more accurately the data.

As the ^{208}Tl background is higher than specified, and topological cut-offs are mainly useful to reject Radon background, the next chapter focuses on setting up a specific technique to reject ^{208}Tl internal background.



(a) $T_{1/2}^{0\nu}$ (90% CL) limits.



(b) $m_{\beta\beta}$ limits.

Figure 3.11: Summary of limits set on $T_{1/2}^{0\nu}$ (a) and $m_{\beta\beta}$ (b) for each case dealt with in this chapter. First-order and optimised topological cut-offs have been applied. Regions of interest have been optimised for each case.

Bibliography

- [1] M. Agostini et al. Probing majorana neutrinos with double- β decay. *Science* 365, 1445, 2019.
- [2] S.I. Alvis et al. Search for neutrinoless double-beta decay in ^{76}Ge with 26 kg-yr of exposure from the majorana demonstrator. *Phys. Rev. C*, 100, 2019.
- [3] O. Azzolini et al. First result on the neutrinoless double- β decay of ^{82}Se with cupid-0. *Phys. Rev. Lett.*, 120:232502, Jun 2018.
- [4] C. Alduino et al. First results from cuore: A search for lepton number violation via $0\nu\beta\beta$ decay of ^{130}Te . *Phys. Rev. Lett.*, 120:132501, Mar 2018.
- [5] J. B. Albert et al. Search for neutrinoless double-beta decay with the upgraded exo-200 detector. *Phys. Rev. Lett.*, 120:072701, Feb 2018.
- [6] A. Gando et al. Search for majorana neutrinos near the inverted mass hierarchy region with kamland-zen. *Phys. Rev. Lett.*, 117:082503, Aug 2016.
- [7] Nucleid database.
- [8] R. Arnold et al. Probing new physics models of neutrinoless double beta decay with supernemo. *Eur. Phys. J. C*, 2010.
- [9] S. Clavez. *Development of reconstruction tools and sensitivity of the SuperNEMO demonstrator*. PhD thesis, Université Paris Sud, 2017.
- [10] Garrido X. Bongrand M. Hamamatsu 8" pmt test in magnetic shield. Internal presentation, 2014.
- [11] Gomez-Cadenas et al. Physics case of supernemo with ^{82}Se source. Internal presentation, 2008.
- [12] R. Arnold et al. Final results on ^{82}Se double beta decay to the ground state of ^{82}Kr from the nemo-3 experiment. *Eur. Phys. J. C*, 2018.
- [13] Tretyak V.I. Ponkratenko O.A. and Zdesenko Yu.G. The event generator decay4 for simulation of doublebeta processes and decay of radioactive nuclei. *Phys. At. Nucl.*, 63:1282–1287, Jul 2000.

- [14] R. Arnold et al. Results of the search for neutrinoless double- β decay in ^{100}mo with the nemo-3 experiment. *Phys. Rev. D*, 2015.
- [15] Perrot F. Radiopurity measurements for 8" pmts and preliminary budget for the sn demonstrator. Internal presentation, 2017.
- [16] Cousins D. Feldman G. A unified approach to the classical statistical analysis of small signals. *Phys.Rev.*, pages 3873–3889, 1999.
- [17] J. Kotila and F. Iachello. Phase-space factors for double- β decay. *Phys. Rev. C*, 85:034316, Mar 2012.
- [18] J. Menéndez et al. Disassembling the nuclear matrix elements of the neutrinoless $\beta\beta$ decay. *Nuclear Physics A*, 818(3):139 – 151, 2009.
- [19] Y. Iwata et al. Large-scale shell-model analysis of the neutrinoless $\beta\beta$ decay of ^{48}Ca . *Phys. Rev. Lett.*, 116:112502, Mar 2016.
- [20] J. Barea, J. Kotila, and F. Iachello. $0\nu\beta\beta$ and $2\nu\beta\beta$ nuclear matrix elements in the interacting boson model with isospin restoration. *Phys. Rev. C*, 91:034304, Mar 2015.
- [21] J. Hyvärinen and J. Suhonen. Nuclear matrix elements for $0\nu\beta\beta$ decays with light or heavy majorana-neutrino exchange. *Phys. Rev. C*, 91:024613, Feb 2015.
- [22] F. Šimkovic et al. $0\nu\beta\beta$ and $2\nu\beta\beta$ nuclear matrix elements, quasiparticle random-phase approximation, and isospin symmetry restoration. *Phys. Rev. C*, 87:045501, Apr 2013.
- [23] Tomás R. Egidio J. Luis Vaquero López N., Rodríguez. Shape and pairing fluctuation effects on neutrinoless double beta decay nuclear matrix elements. *Phys. Rev. Lett.*, 111:142501, Sep 2013.
- [24] J. M. Yao, L. S. Song, K. Hagino, P. Ring, and J. Meng. Systematic study of nuclear matrix elements in neutrinoless double- β decay with a beyond-mean-field covariant density functional theory. *Phys. Rev. C*, 91:024316, Feb 2015.
- [25] P. K. Rath, R. Chandra, K. Chaturvedi, P. K. Raina, and J. G. Hirsch. Uncertainties in nuclear transition matrix elements for neutrinoless $\beta\beta$ decay within the projected-hartree-fock-bogoliubov model. *Phys. Rev. C*, 82:064310, Dec 2010.
- [26] Dong-Liang Fang, Amand Faessler, Vadim Rodin, and Fedor Šimkovic. Neutrinoless double- β decay of deformed nuclei within quasiparticle random-phase approximation with a realistic interaction. *Phys. Rev. C*, 83:034320, Mar 2011.
- [27] Loaiza P. Source foils measurement with bipo. Internal presentation, 2017.

- [28] Xin Ran Liu. Radon mitigation strategy and results for the supernemo experiment. IoP APP / HEPP Conference, 2018.
- [29] A. Chapon. *Mesure des processus de double désintégration bêta du Mo vers l'état excité 0_1^+ du Ru dans l'expérience Nemo3, Programme de R&D SuperNEMO : mise au point d'un détecteur BiPo pour la mesure de très faibles contaminations de feuilles sources*. PhD thesis, Université Caen Basse-Normandie, 2011.
- [30] Snow S. A magnetic field map for the tracker. Internal presentation, 2015.
- [31] A. Pin. *Recherche de la nature du neutrino via la décroissance double bêta sans émission de neutrinos. Caractérisation et optimisation du calorimètre SuperNEMO et impact sur la recherche de la décroissance du 82Se* . Développement du premier prototype LiquidO. PhD thesis, Université Bordeaux-Gradignan, 2020.
- [32] A. H. Wapstra G. Audi. The 1995 update to the atomic mass evaluation. *Nucl. Phys. A*, 595:409–480, feb 1995.
- [33] Dassié D. et al. Two-neutrino double- β decay measurement of ^{100}Mo . *Phys. Rev. D*, 51:2090–2100, Mar 1995.
- [34] R. Arnold et al. Measurement of the $2\nu\beta\beta$ decay half-life of ^{150}Nd and a search for $0\nu\beta\beta$ decay processes with the full exposure from the nemo-3 detector. *Phys. Rev. D*, 94, oct 2016.